



New Parallaxes of Galactic Cepheids from Spatially Scanning the *Hubble Space Telescope*: Implications for the Hubble Constant

Adam G. Riess^{1,2}, Stefano Casertano^{1,2}, Wenlong Yuan^{2,3} , Lucas Macri³ , Jay Anderson¹ , John W. MacKenty¹, J. Bradley Bowers², Kelsey I. Clubb⁴, Alexei V. Filippenko^{4,5,6} , David O. Jones² , and Brad E. Tucker⁴

¹ Space Telescope Science Institute, 3700 San Martin Drive, Baltimore, MD 21218, USA

² Department of Physics and Astronomy, Johns Hopkins University, Baltimore, MD 21218, USA

³ Texas A&M University, Department of Physics and Astronomy, College Station, TX, USA

⁴ Department of Astronomy, University of California, Berkeley, CA 94720-3411, USA

⁵ Miller Institute for Basic Research in Science, University of California, Berkeley, USA

Received 2017 December 21; revised 2018 February 1; accepted 2018 February 5; published 2018 March 16

Abstract

We present new measurements of the parallax of seven long-period (≥ 10 days) Milky Way (MW) Cepheid variables (SS CMa, XY Car, VY Car, VX Per, WZ Sgr, X Pup, and S Vul) using one-dimensional astrometric measurements from spatial scanning of Wide-Field Camera 3 on the *Hubble Space Telescope* (*HST*). The observations were obtained at ~ 6 month intervals over 4 years. The distances are 1.7–3.6 kpc, with a mean precision of $45 \mu\text{as}$ (signal-to-noise ratio (S/N) ≈ 10) and a best precision of $29 \mu\text{as}$ ($S/N = 14$). The accuracy of the parallaxes is demonstrated through independent analyses of > 100 reference stars. This raises to 10 the number of long-period Cepheids with significant parallax measurements, 8 obtained from this program. We also present high-precision mean $F555W$, $F814W$, and $F160W$ magnitudes of these Cepheids, allowing a direct, zeropoint-independent comparison to > 1800 extragalactic Cepheids in the hosts of 19 SNe Ia. This sample addresses two outstanding systematic uncertainties affecting prior comparisons of MW and extragalactic Cepheids used to calibrate the Hubble constant (H_0): their dissimilarity of periods and photometric systems. Comparing the new parallaxes to their predicted values derived from reversing the distance ladder gives a ratio (or independent scale for H_0) of 1.037 ± 0.036 , consistent with no change and inconsistent at the 3.5σ level with a ratio of 0.91 needed to match the value predicted by *Planck* cosmic microwave background data in concert with ΛCDM . Using these data instead to augment the Riess et al. measurement of H_0 improves the precision to 2.3%, yielding $73.48 \pm 1.66 \text{ km s}^{-1} \text{ Mpc}^{-1}$, and the tension with *Planck* + ΛCDM increases to 3.7σ . The future combination of *Gaia* parallaxes and *HST* spatial scanning photometry of 50 MW Cepheids can support a $< 1\%$ calibration of H_0 .

Key words: astrometry – cosmological parameters – distance scale – parallaxes – stars: distances – stars: variables: Cepheids

1. Introduction

The Hubble constant (H_0) measured locally and the sound horizon observed from the cosmic microwave background radiation (CMB) provide the two chief absolute scales at opposite ends of the visible expansion history of the universe. Comparing the two gives a stringent end-to-end test of ΛCDM (the cosmological constant plus cold dark matter in a flat universe), the new “Standard Model” of cosmology, over the full history of the universe (Bernal et al. 2016). By steadily improving the precision and accuracy of the H_0 measurement from Cepheids and Type Ia supernovae (SNe Ia), evidence has been growing of a significant discrepancy between the two. The local and direct determination of H_0 from Riess et al. (2016, hereafter R16) gives $H_0 = 73.24 \pm 1.74 \text{ km s}^{-1} \text{ Mpc}^{-1}$ and the most recent value from Planck Collaboration et al. (2016) in concert with ΛCDM is $66.93 \pm 0.62 \text{ km s}^{-1} \text{ Mpc}^{-1}$, a 3.4σ difference.

Intriguingly, this discrepancy does not appear to be attributable to an error in any one source of data, either in the local determination of H_0 or from the CMB. Reanalyses of the R16 data have shown minimal differences in the local determination of H_0 with values ranging within $\pm 1\%$, well within its full 2.4% uncertainty (Cardona et al. 2017; Feeney et al. 2017; Follin & Knox 2017). The discrepancy remains

significant using any one of three independent, geometric approaches commonly used to calibrate the luminosities of Cepheids along the distance ladder: masers in NGC 4258 (Humphreys et al. 2013), detached eclipsing binaries (DEBs) in the Large Magellanic Cloud (LMC; Pietrzyński et al. 2013), or trigonometric parallaxes of Milky Way (MW) Cepheids (Benedict et al. 2007; van Leeuwen et al. 2007; Riess et al. 2014; Casertano et al. 2016). Replacing Cepheids with the tip of the red giant branch to reach SN Ia hosts, when possible, produces changes of $< 0.5\%$ for the same sources (Jang & Lee 2017; Jang et al. 2017), as does replacing SN Ia distance estimates based on optical magnitudes with those relying on the dust-insensitive near-infrared (NIR; Dhawan et al. 2017). Indeed, replacing the entire distance ladder with another local universe distance estimator, time delays from strong gravitational lensing, confirms and reinforces the discrepancy with $H_0 = 72.8 \pm 2.4 \text{ km s}^{-1} \text{ Mpc}^{-1}$ for realistic values of Ω_M (Bonvin et al. 2017).

At the early-universe end of the comparison, Addison et al. (2017) have shown that the *Planck* data can be replaced with measurements of Ω_B via the observed deuterium abundance to calibrate baryon acoustic oscillations with no significant change, yielding a predicted value of $H_0 = 67.0 \pm 1.2 \text{ km s}^{-1} \text{ Mpc}^{-1}$ (but see also Aylor et al. 2017; DES Collaboration et al. 2017). Yet because this discrepancy may ultimately be interpreted as evidence of new physics in the

⁶ Miller Senior Fellow.

cosmological model, the burden of proving that it is not the result of a measurement error is necessarily high.

Here we present new trigonometric parallax measurements of MW Cepheids using the spatial scanning technique of Riess et al. (2014) and Casertano et al. (2016). These measurements address two outstanding systematic uncertainties associated with prior comparisons of MW and extragalactic Cepheids on the distance ladder: their dissimilarity of periods and photometric systems. The astrometric precision of spatial scanning enables parallax measurements at $D > 2$ kpc, where most Cepheids with periods of $P > 10$ days live, the period range visible for those in distant SN Ia hosts. As we show, scanning is also superior to the staring mode for obtaining the precise magnitudes of bright MW Cepheids on the same photometric system as their extragalactic brethren.

Cepheid variables continue to be the most useful primary distance indicator because they are common, they are sufficiently luminous to be seen with the *Hubble Space Telescope* (*HST*) in the hosts of nearby SNe Ia ($D \approx 20\text{--}40$ Mpc), and they yield an individual distance precision of 0.07 mag (Persson et al. 2004; Macri et al. 2015) when observed in the NIR, where they are also insensitive to metallicity (Wielgorski et al. 2017). As observed with *HST* in the hosts of SNe Ia at $D \approx 20\text{--}40$ Mpc, the reduction in their individual precision ($\sim 0.3\text{--}0.4$ mag) due to surface brightness fluctuations in their hosts is offset by typically visible sample sizes of ~ 100 per host, providing a mean distance error (statistical) below the uncertainty of the individual SNe Ia they calibrate (~ 0.1 mag).

Initially, the use of Cepheids as absolute distance indicators was severely limited by an inability to calibrate their luminosity, once a source of egregious error (Hubble 1929). Attaining this calibration demands model-independent, geometric distance measures to the locations of known Cepheids. Even the nearest known Cepheid (oscillating in the fundamental mode), δ Cep, has a parallax of only a few mas, requiring sub-mas measurements for useful limits (Gatewood et al. 1993). The most precise previous measurements of stellar parallax came from the Fine Guidance Sensor (FGS) on *HST*, which can measure relative astrometry to a typical precision of $\sim 0.2\text{--}0.3$ mas and thus could usefully measure trigonometric parallaxes to ~ 10 known MW Cepheids within 0.5 kpc (Benedict et al. 2007). Unfortunately, only two of these have $P \geq 10$ days, the lower end of the period range of those measurable at the typical distances of SN Ia hosts. Cepheid parallax measurements from *Gaia* show tremendous promise and will likely revolutionize such measurements by the mission’s final data release in ~ 2022 . The first MW Cepheid parallaxes available from *Gaia* DR1 have a mean uncertainty of $\sigma \approx 0.3$ mas and parallax $S/N \approx 1$ (Lindegren et al. 2016). Although the mean of all ~ 200 Cepheids has been used to test and confirm the local measurement of H_0 , it may not be possible to average so many measurements without incurring additional systematic uncertainties (Casertano et al. 2017).

The previously mentioned Cepheid calibrations from the LMC and NGC 4258 have specific limitations that continue to motivate the pursuit of MW Cepheid parallaxes. The LMC is a dwarf galaxy where the environment is quite different from the large spiral hosts used to calibrate SNe Ia with Cepheids; its Cepheids are more metal-poor by 0.3–0.4 dex (Romaniello et al. 2008). As for NGC 4258, its maser distance is unlikely to improve, limiting the ultimate precision available from this anchor to 2.6% (Riess et al. 2016). Advancements in the

observations of Cepheid trigonometric parallaxes are critical to test the current tension in H_0 and to support the future goal of measuring it to 1% precision.

This is the third paper in a sequence developing and employing a new technique for measuring stellar parallax using spatial scanning observations with the Wide Field Camera 3 (WFC3) on *HST*. We refer the reader to the first (Riess et al. 2014, hereafter Paper I) and second applications (Casertano et al. 2016, hereafter Paper II), which provide a thorough description of how spatial scan astrometric data are obtained, calibrated, and analyzed to reach a measurement precision as small as ~ 30 μ as. Here we provide only a brief overview of the method.

To produce a meaningful measurement ($S/N \approx 10$) of the parallax of $P > 10$ day Cepheids, nearly all of which have $D > 2$ kpc, it is necessary to reach an astrometric precision of ~ 30 μ as for individual epochs of MW Cepheids. This is a factor of 45 better than the ESA astrometric mission *Hipparcos* mean for all $P > 10$ day MW Cepheids ($\sigma = 1.4$ mas; van Leeuwen et al. 2007), and an order of magnitude better than typically possible with the FGS on *HST* or from staring mode observations with WFC3. For bright sources (MW Cepheids at $D \approx 3$ kpc have $V \approx 9$ mag), spatial scanning⁷ provides multiple advantages. In order of decreasing importance, these are (1) a factor of 1000 higher statistical sampling from full detector scans, (2) the ability to average the signal across uncorrected, local distortions along the detector, and (3) removal of jitter along the measurement direction through the comparison to reference-star scans. These advantages together provide the means to measure parallaxes with 30 μ as precision as described in Papers I and II. A fourth advantage occurs in the use of Cepheids to measure H_0 : the ability to measure photometry of MW Cepheids with the same photometric system as those in SN Ia hosts to cancel zeropoint uncertainties while avoiding additional uncertainties from detector saturation, undersampling and flat-field variations.

Here we present a sample of seven Cepheids, each of which has been observed over 4 years with eight to nine epochs separated by 6 months, double the time span available in Papers I and II and for a much larger sample. In Section 2, we present the spatial scanning measurements and determinations of parallax, and Section 3 gives the spatial scanning *HST* photometry of these Cepheids. We use the prior data in Section 4 to test the scale of the local determination of H_0 and to improve the calibration of the MW Cepheid period-luminosity (P - L) relation. In Section 5, we discuss the implications and additional considerations.

The *HST* data used in this paper are available at [doi:10.17909/T9QM3G].

2. Parallax Measurements from Spatial Scans

The process of extracting high-precision relative astrometry from star trails in spatial scans is described in detail in Papers I and II, and we direct the reader there for further information. Here we review the key steps discussed in these papers.

1. Spatial scans are obtained along the detector Y axis with a 0.05° tilt to vary the pixel phase of a point-spread function (PSF) by 1 pixel per 200 pixels scanned. Astrometric measurements are made along a single dimension, the

⁷ While shift-and-stare observations using hundreds of exposures could accomplish this as well, readout times and onboard storage limitations make this kind of observing impractical.

- detector X axis, by fitting a previously determined position-dependent line-spread function (LSF) to each 15 pixel minirow along a star scan, resulting in measurements of the source X position as a function of the Y scan position.
2. Astrometric measurements are obtained from deep and shallow scans of the field containing the Cepheid. The deep scans provide astrometry of fainter reference stars and the shallow scans measure the brighter Cepheids without saturation. Stars of intermediate brightness ($11 < V < 15$ mag) are used to register the two.
 3. Pixels struck by cosmic rays and known bad pixels (from prior maps) are excluded from the minirow fits, as are rows whose astrometric measurements in the X direction would be expected to be biased by more than 1 millipixel owing to a nearby star trail (as estimated from their separation and relative brightness).
 4. Epochs are separated by ~ 6 months when the field can be observed by *HST* at nominal or $\pm 180^\circ$ orientation, while maintaining the relative separations of star trails.
 5. Relative detector coordinates are transformed to relative sky coordinates using a geometric distortion solution following Bellini et al. (2011) specific to the scan filter. Additional corrections are made for time-dependent plate-scale variations due to velocity aberration, frame-to-frame rotation, and variable field rotation along the scan. Lastly, the relative astrometry from independent, coeval scans is registered using a two-dimensional (2D) second-order polynomial, $f(x, y) = \Delta X$, to account for simple time-dependent distortions along the measurement direction.
 6. Relative astrometry along one dimension is measured as the difference from an average, four-times-oversampled reference line, constructed from the superposition of all time-aligned scan lines. The reference line contains the jitter history, length, and slope of the scan.
 7. An additional static perturbation to the geometric distortion solution from Bellini et al. (2011) was computed for three filters ($F606W$, $F621M$, and $F673N$) based on repeated scans of stars in M48 and M67 (GO 14394), and applied as described in Paper II.
 8. Repeated scans demonstrate measurement precision (i.e., residuals) for well-sampled bright stars at the 0.5–2 millipixel level (20–80 μ as), with the higher precision obtained for scans with similar conditions (orient, position along breathing-focus cycle) and lesser precision for scans with orients differing by 180° .
 9. A multisource, multiparameter model is fit simultaneously to the Cepheid and the reference stars in the field using as additional constraints the spectrophotometric (hereafter SP) parallax priors for the reference stars. These priors are derived from the comparison of stellar magnitudes from *HST* in typically two UV filters ($F275W$, $F336W$), four Strömgren medium bands ($F410M$, $F467M$, $F547M$, $F621M$), two NIR bands ($F850LP$, $F160W$), as well as catalog 2MASS *JHK* and *Wide-field Infrared Survey Explorer* (*WISE*) Band-1 and Band-2 magnitudes. In addition, the stellar model for a reference star is constrained with spectra that are used to determine the MK spectral class and luminosity class of each star (Gray & Corbally 2014), which constrains their temperature and specific gravity. A best-fitting stellar model for each star is determined from the Padova Isocrones (Bressan et al. 2012) dependent on three

physical parameters (temperature, log gravity, metallicity) and two environmental parameters (extinction and distance). A line-of-sight, one-dimensional (1D) extinction probability prior for stars along the line of sight based on 2MASS data (Marshall et al. 2006) augments the fits, as does a model of the frequency of the stellar types along each line of sight for the MW (Robin et al. 2003). The reference stars in each field are found to have a mean distance of $\mu = 11.7\text{--}12.0$ mag with a mean individual uncertainty of ~ 0.2 mag. The typical error in the reduction from relative to absolute parallax is $\sim 10 \mu\text{as}$ (Paper II) and is found to be subdominant to the astrometric measurement errors.

10. Each star's 1D motion is modeled as the superposition of a relative proper motion and parallax. Stars whose eight to nine epochs (4 years span) poorly fit this model (e.g., astrometric binaries), typically $\sim 10\%$ –20% of all stars, are iteratively rejected until the fit converges. Extensive observations of high-precision radial velocities were used by Anderson et al. (2016) to rule out significant contamination of the parallax measurements (an upper limit of $< 4\%$) due to binarity for the Cepheids presented here.
11. The global fit makes use of the parallax factors or the projection of the parallax ellipse on the X -axis of the detector at the measurement epoch. By definition, the parallax factors are a number between -1.0 and 1.0 , and in practice they have a mean absolute value of 0.8 .

In Table 1, we list the observations for each Cepheid field. Figures 1–7 show the reference stars and Cepheid in each field. Table 2 lists the parameters and characteristics of the reference stars in each of the Cepheid fields.

As in Paper II, we test the fidelity of our astrometric parallax determinations by comparing them to the SP parallax priors for the reference stars. To make this comparison independent of the SP measurement, we remove each from the set of prior constraints before recomputing the best global fit. The resulting astrometric parallax is then compared to its independent SP parallax. These are shown for all of the reference stars in Figure 8. On average, the agreement is quite good. We note that the astrometric parallax measurement for the Cepheid has the advantage of using all of the reference-star SP priors or one more than these tests for the reference stars.

In Figure 9, we display the proper-motion-subtracted astrometric measurements of the Cepheids and their best-fit parallaxes. We give the Cepheid parallaxes and their uncertainties in Table 3, showing the contribution from the reduction from relative to absolute parallax, which is subdominant in all cases. Differences in the Cepheid parallax uncertainties are largely produced by the differing availability of uncontaminated reference stars used to register deep and shallow scans as discussed further in Section 5.⁸

⁸ The process of astrometrically registering shallow and deep scans while retaining a precision of a few millipixels necessitates the determination of seven free parameters including an offset, frame rotation, and five polynomial parameters to solve for second-order in x (time-dependent geometric distortions likely due to the thermal cycle of the telescope). Thus, a robust solution requires more than seven reference stars with high S/Ns in both scans, not saturated in the deep scan, running most of the scan length, and not crossing another star trail. Unfortunately, a number of the Cepheids initially targeted for spatial scanning do not have this number of reference stars and their monitoring was curtailed after five epochs. In the future, an ability to predict the distortion produced by the thermal cycle could reduce the number of necessary stars to $\sim 2\text{--}3$ and allow a complete analysis of all observed Cepheids with improved relative astrometry.

Table 1
Spatial Scanning Observations Used in This Paper

Epoch	Date	Program ID	Scan Rates ("/sec)	Filters	Scan Lengths (")	PA V3 (deg)	X pos targ (")	File Root
sscma								
1	2012 Oct 23	12879	0.330 0.330	<i>F</i> 606 <i>W</i> <i>F</i> 621 <i>M</i>	115.5 115.5	116.00	-3.10 -2.99	ibzc04
1	2012 Oct 23	12879	1.505	<i>F</i> 606 <i>W</i>	526.7	116.00	-2.14	ibzc04
2	2013 Apr 18	12879	0.330 0.330	<i>F</i> 606 <i>W</i> <i>F</i> 621 <i>M</i>	114.8 114.8	295.99	-3.10 -2.99	ibzc15
2	2013 Apr 18	12879	1.505	<i>F</i> 606 <i>W</i>	523.7	295.99	-2.13	ibzc15
3	2013 Oct 22	13344	0.330 0.330	<i>F</i> 606 <i>W</i> <i>F</i> 621 <i>M</i>	114.8 114.8	116.00	-3.10 -2.99	ic8z04
3	2013 Oct 22	13344	1.505	<i>F</i> 606 <i>W</i>	523.7	116.00	-2.13	ic8z04
4	2014 Apr 16	13344	0.330 0.330	<i>F</i> 606 <i>W</i> <i>F</i> 621 <i>M</i>	114.8 114.8	295.99	2.898 3.000	ic8z15
4	2014 Apr 16	13344	1.505	<i>F</i> 606 <i>W</i>	523.7	295.99	9.860	ic8z15
5	2014 Oct 23	13678	0.330 0.330	<i>F</i> 606 <i>W</i> <i>F</i> 621 <i>M</i>	114.8 114.8	116.00	-3.10 -3.10	icir03
7	2015 Oct 23	14206	0.330 0.330	<i>F</i> 606 <i>W</i> <i>F</i> 621 <i>M</i>	114.8 114.8	116.00	-3.10 -2.99	ictn06
7	2015 Oct 23	14206	1.505	<i>F</i> 606 <i>W</i>	523.7	116.00	-2.13	ictn06
8	2016 Apr 15	14206	0.330 0.330	<i>F</i> 606 <i>W</i> <i>F</i> 621 <i>M</i>	114.8 114.8	295.99	2.898 3.000	ictn07
8	2016 Apr 15	14206	1.505	<i>F</i> 606 <i>W</i>	523.7	295.99	17.86	ictn07
9	2016 Oct 22	14648	0.330 0.330	<i>F</i> 606 <i>W</i> <i>F</i> 621 <i>M</i>	114.8 114.8	116.00	-3.10 -3.10	id5d06
9	2016 Oct 22	14648	0.330	<i>F</i> 606 <i>W</i>	114.8	115.99	-2.99	id5d06
a	2017 Apr 14	14648	0.330 0.330	<i>F</i> 606 <i>W</i> <i>F</i> 621 <i>M</i>	114.8 114.8	295.99	2.898 3.000	id5d11
a	2017 Apr 14	14648	1.505	<i>F</i> 606 <i>W</i>	523.7	295.99	17.86	id5d11
xycar								
1	2012 Aug 07	12879	0.410 0.410	<i>F</i> 606 <i>W</i> <i>F</i> 621 <i>M</i>	143.5 143.5	337.01	-3.12 -2.99	ibzc02
2	2013 Jan 26	12879	0.410 0.430	<i>F</i> 606 <i>W</i> <i>F</i> 621 <i>M</i>	143.5 149.6	156.98	-3.12 -2.99	ibzc11
3	2013 Aug 08	13344	0.410 0.410	<i>F</i> 606 <i>W</i> <i>F</i> 621 <i>M</i>	143.5 143.5	337.01	-3.12 -2.99	ic8z02
4	2014 Jan 25	13344	0.410 0.430	<i>F</i> 606 <i>W</i> <i>F</i> 621 <i>M</i>	142.6 149.6	156.98	2.873 3.001	ic8z11
5	2014 Aug 07	13678	0.410 0.410	<i>F</i> 606 <i>W</i> <i>F</i> 621 <i>M</i>	143.5 143.5	337.01	-3.12 -3.12	icir01
7	2015 Aug 09	14206	0.410 0.410	<i>F</i> 606 <i>W</i> <i>F</i> 621 <i>M</i>	143.5 143.5	337.01	-3.12 -2.99	ictn01
8	2016 Jan 27	14206	0.410 0.410	<i>F</i> 606 <i>W</i> <i>F</i> 621 <i>M</i>	143.5 143.5	156.98	2.872 3.001	ictn02
9	2016 Aug 09	14648	0.410 0.410	<i>F</i> 606 <i>W</i> <i>F</i> 621 <i>M</i>	143.5 143.5	337.01	-3.12 -3.12	id5d01
a	2017 Jan 22	14648	0.410 0.410	<i>F</i> 606 <i>W</i> <i>F</i> 621 <i>M</i>	143.5 143.5	156.98	2.872 3.001	id5d22
vxper								
1	2013 Feb 07	12879	0.410 0.430	<i>F</i> 606 <i>W</i> <i>F</i> 621 <i>M</i>	143.5 150.5	250.02	-3.12 -2.99	ibzc13
2	2013 Aug 28	12879	0.410 0.430	<i>F</i> 606 <i>W</i> <i>F</i> 621 <i>M</i>	143.5 150.5	69.971	-3.12 -2.99	ibzc23
3	2014 Feb 09	13344	0.410 0.430	<i>F</i> 606 <i>W</i> <i>F</i> 621 <i>M</i>	143.5 150.5	250.02	-3.12 -2.99	ic8z13
4	2014 Aug 17	13344	0.410 0.430	<i>F</i> 606 <i>W</i> <i>F</i> 621 <i>M</i>	142.6 149.6	69.970	2.873 3.001	ic8z23
5	2015 Feb 09	13678	0.410 0.430	<i>F</i> 606 <i>W</i> <i>F</i> 621 <i>M</i>	143.5 150.5	250.02	-3.12 -3.13	icir11
6	2015 Aug 17	14206	0.410 0.430	<i>F</i> 606 <i>W</i> <i>F</i> 621 <i>M</i>	142.6 149.6	69.970	2.873 3.001	ictn05
7	2016 Feb 07	14206	0.410 0.430	<i>F</i> 606 <i>W</i> <i>F</i> 621 <i>M</i>	142.6 149.6	250.02	-3.12 -2.99	ictn08
8	2016 Aug 27	14648	0.410 0.430	<i>F</i> 606 <i>W</i> <i>F</i> 621 <i>M</i>	142.6 149.6	69.970	2.873 2.867	id5d05
9	2017 Feb 07	14648	0.410 0.430	<i>F</i> 606 <i>W</i> <i>F</i> 621 <i>M</i>	142.6 149.6	250.02	-3.12 -2.99	id5d23
wzsgr								
1	2013 Sep 24	13334	0.410 0.430	<i>F</i> 606 <i>W</i> <i>F</i> 673 <i>N</i>	143.5 149.6	288.99	-3.12 -3.13	ic8k13
2	2014 Mar 25	13334	0.410 0.430	<i>F</i> 606 <i>W</i> <i>F</i> 673 <i>N</i>	143.5 149.6	109.00	-3.12 -3.13	ic8k14
3	2014 Sep 23	13686	0.410 0.430	<i>F</i> 606 <i>W</i> <i>F</i> 673 <i>N</i>	143.5 149.6	288.99	-3.12 -3.13	iciu13
4	2015 Mar 25	13686	0.410 0.430	<i>F</i> 606 <i>W</i> <i>F</i> 673 <i>N</i>	143.5 149.6	109.00	-3.12 -3.13	iciu23
5	2015 Sep 23	14062	0.410 0.430	<i>F</i> 606 <i>W</i> <i>F</i> 673 <i>N</i>	143.5 149.6	288.99	-3.12 -3.13	ict704
6	2016 Mar 25	14206	0.410 0.430	<i>F</i> 606 <i>W</i> <i>F</i> 673 <i>N</i>	143.5 149.6	109.00	-3.12 -3.13	ictn14
7	2016 Sep 24	14206	0.410 0.430	<i>F</i> 606 <i>W</i> <i>F</i> 673 <i>N</i>	143.5 149.6	288.99	-3.12 -3.13	ictn13
8	2017 Mar 25	14648	0.410 0.430	<i>F</i> 606 <i>W</i> <i>F</i> 673 <i>N</i>	143.5 149.6	109.00	-3.12 -3.13	id5d14
svul								
1	2013 Oct 29	13334	0.410 0.690	<i>F</i> 606 <i>W</i> <i>F</i> 621 <i>M</i>	143.5 241.5	277.00	-3.12 -0.99	ic8k03
2	2014 Mar 28	13334	0.410 0.690	<i>F</i> 606 <i>W</i> <i>F</i> 621 <i>M</i>	143.5 241.5	96.993	2.872 5.002	ic8k04
3	2014 Oct 26	13686	0.410 0.690	<i>F</i> 606 <i>W</i> <i>F</i> 621 <i>M</i>	143.5 241.5	277.00	-3.12 -0.99	iciu17
4	2015 Mar 30	13686	0.410 0.690	<i>F</i> 606 <i>W</i> <i>F</i> 621 <i>M</i>	143.5 241.5	96.993	2.872 5.002	iciu18
5	2015 Oct 29	14062	0.410 0.690	<i>F</i> 606 <i>W</i> <i>F</i> 621 <i>M</i>	143.5 241.5	277.00	-3.12 -0.99	ict706
6	2016 Mar 28	14206	0.410 0.690	<i>F</i> 606 <i>W</i> <i>F</i> 621 <i>M</i>	143.5 241.5	96.993	2.872 10.00	ictn16
7	2016 Oct 25	14206	0.410 0.690	<i>F</i> 606 <i>W</i> <i>F</i> 621 <i>M</i>	143.5 241.5	277.00	-3.12 -0.99	ictn15
8	2017 Mar 28	14648	0.410 0.690	<i>F</i> 606 <i>W</i> <i>F</i> 621 <i>M</i>	143.5 241.5	96.993	2.872 10.00	id5d15

Table 1
(Continued)

Epoch	Date	Program ID	Scan Rates ("/sec)	Filters	Scan Lengths (")	PA V3 (deg)	X pos targ (")	File Root
xpup								
1	2013 Oct 24	13334	0.410 0.350	<i>F</i> 606 <i>W</i> <i>F</i> 673 <i>N</i>	143.5 129.5	122.00	-3.12 -3.11	ic8k11
2	2014 Apr 16	13334	0.410 0.350	<i>F</i> 606 <i>W</i> <i>F</i> 673 <i>N</i>	143.5 129.5	301.99	-3.12 -3.11	ic8k12
3	2014 Oct 24	13686	0.410 0.350	<i>F</i> 606 <i>W</i> <i>F</i> 673 <i>N</i>	143.5 129.5	122.00	-3.12 -3.11	iciu21
4	2015 Apr 18	13686	0.410 0.350	<i>F</i> 606 <i>W</i> <i>F</i> 673 <i>N</i>	143.5 129.5	301.99	-3.12 -3.11	iciu22
5	2015 Oct 24	14062	0.410 0.350	<i>F</i> 606 <i>W</i> <i>F</i> 673 <i>N</i>	143.5 129.5	122.00	-3.12 -3.11	ict707
6	2016 Apr 16	14206	0.410 0.350	<i>F</i> 606 <i>W</i> <i>F</i> 673 <i>N</i>	143.5 129.5	301.99	-3.12 -3.11	ictn18
7	2016 Oct 23	14206	0.410 0.350	<i>F</i> 606 <i>W</i> <i>F</i> 673 <i>N</i>	143.5 129.5	122.00	-3.12 -3.11	ictn17
8	2017 Apr 16	14648	0.410 0.350	<i>F</i> 606 <i>W</i> <i>F</i> 673 <i>N</i>	143.5 129.5	301.99	-3.12 -3.11	id5d16
vycar								
1	2013 Jul 09	13334	0.410 0.860	<i>F</i> 606 <i>W</i> <i>F</i> 673 <i>N</i>	143.5 301.0	327.00	-3.12 -0.99	ic8k07
2	2014 Jan 10	13334	0.410 0.860	<i>F</i> 606 <i>W</i> <i>F</i> 673 <i>N</i>	143.5 301.0	146.99	2.872 5.003	ic8k08
3	2014 Jul 28	13686	0.410 0.860	<i>F</i> 606 <i>W</i> <i>F</i> 673 <i>N</i>	143.5 301.0	327.00	-3.12 -0.99	iciu07
4	2015 Jan 12	13686	0.410 0.860	<i>F</i> 606 <i>W</i> <i>F</i> 673 <i>N</i>	143.5 301.0	146.99	2.872 5.003	iciu20
5	2015 Jul 07	14062	0.410 0.860	<i>F</i> 606 <i>W</i> <i>F</i> 673 <i>N</i>	143.5 301.0	327.00	-3.12 -0.99	ict703
6	2016 Jan 10	14206	0.410 0.860	<i>F</i> 606 <i>W</i> <i>F</i> 673 <i>N</i>	143.5 301.0	146.99	2.872 9.003	ictn12
7	2016 Jul 07	14206	0.410 0.860	<i>F</i> 606 <i>W</i> <i>F</i> 673 <i>N</i>	143.5 301.0	327.00	-3.12 -0.99	ictn19
8	2017 Jan 12	14648	0.410 0.860	<i>F</i> 606 <i>W</i> <i>F</i> 673 <i>N</i>	143.5 301.0	146.99	2.872 9.003	id5d13

Note. There are two exposures for each unique entry except the $1.^{\prime\prime}5 \text{ s}^{-1}$ scans for sscma. All exposure times are 348–350 s.

3. Rapid Scan WFC3 System Photometry

The best way to reduce the propagation of zeropoint and bandpass uncertainties among Cepheid flux measurements along the distance ladder is to observe all Cepheids with a single, stable photometric system. This is especially important in the NIR, where individual system zeropoint uncertainties are $\sim 0.02\text{--}0.03$ mag (Riess 2011) and the relative differences between two systems is thus $\sim 0.03\text{--}0.04$ mag. This is challenging to accomplish for MW Cepheids, which are 14–18 mag brighter than their extragalactic counterparts.

Spatial scanning offers several advantages to achieve this goal. Scanning varies the position of the source on the detector, which averages down errors in the flat fields and can also be used to vary the pixel phase, reducing the uncertainty from undersampled PSF photometry. By scanning at high speeds, it is possible to reliably reduce the effective exposure time far below what is possible in staring mode owing to variations and uncertainties in shutter flight time (Sahu et al. 2015).

To observe these MW Cepheids in the range of $7 < V < 10$ mag, we utilized the highest available scan speeds of $7.^{\prime\prime}5 \text{ s}^{-1}$ (under gyro control) in *F*160*W* to realize an effective exposure time of ~ 0.01 s. In *F*555*W* and *F*814*W* scan speeds were either $7.^{\prime\prime}5 \text{ s}^{-1}$ or $4.^{\prime\prime}0 \text{ s}^{-1}$.

Photometry is measured from the amplitude of the fit of the LSF to the extracted signal in each 15 pixel minirow, which is the same fit used for the astrometric measurement of the source’s position along the *X* direction—divided by the effective exposure time (i.e., the pixel size divided by the scan rate). Empirical measurements of the scan rate show very good agreement with the commanded rate, with the latter preferred, as it is less noisy. However, as we will show, we use pairs of direct and scanning images to calibrate out a possible error in the pixel size and scan rate.

Because of the variable geometric distortion, two corrections must be applied to convert this amplitude into a uniform flux measurement across the detector, unaffected by the local pixel

size. The first is to multiply the measured flux by the local (relative) pixel area using the same pixel area map (or distortion solution to rectify images) used for photometry of all point sources in the staring mode.⁹ The second is a correction for the different size of each pixel along the scan (*Y*) direction: larger pixels take longer to be traversed, and thus experience a longer effective exposure time. The second correction partially compensates the first, so that no correction is actually needed for the pixel size along *Y*, and the net correction needed is to multiply the fitted amplitude by the relative pixel size in the *X* direction.

By comparing pairs of scans of MW Cepheids (programs GO-13335, GO-13928) in back-to-back exposures, we find a mean photometric error per scan observation of 0.007, 0.003, and 0.001 mag in *F*160*W*, *F*555*W*, and *F*814*W*, respectively. The onset of saturation at $7.^{\prime\prime}5 \text{ s}^{-1}$ occurs for stars brighter than 7.2, 6.8, and 5.6 (Vega) mag in *F*160*W*, *F*555*W*, and *F*814*W*, respectively. Within 1 mag (brighter) of this saturation limit, the precision of spatial scan photometry is seen to decrease to 0.01–0.02 mag in *F*555*W* and 0.003–0.01 mag in *F*814*W*. The precision in *F*160*W* does not significantly decrease within 2 mag (brighter) of the onset of saturation. In general, photometry of mildly saturated Cepheids (i.e., loss of the central 2–3 pixels) remains robust and well constrained in these scans (also seen in comparison to ground-based observations) because of good knowledge of the WFC3 PSF, the stability of WFC3, the natural averaging of measurements over position on the detector, and the variation in source pixel phase, which mitigates undersampling of the PSF.

To insure uniformity between photometry in imaging modes, we use a large set of images of reference stars obtained in pairs, one staring and one scanning, to find and measure the offset between the two. We expect a constant-magnitude offset as it

⁹ A pixel area map is used to normalize the flux for photometry to compensate for the fact that the flat field for WFC3 images is defined so that a uniform illumination produces equal counts per pixel, regardless of their size. Therefore, the local measured count rate is actually proportional to the flux per unit area on the sky.

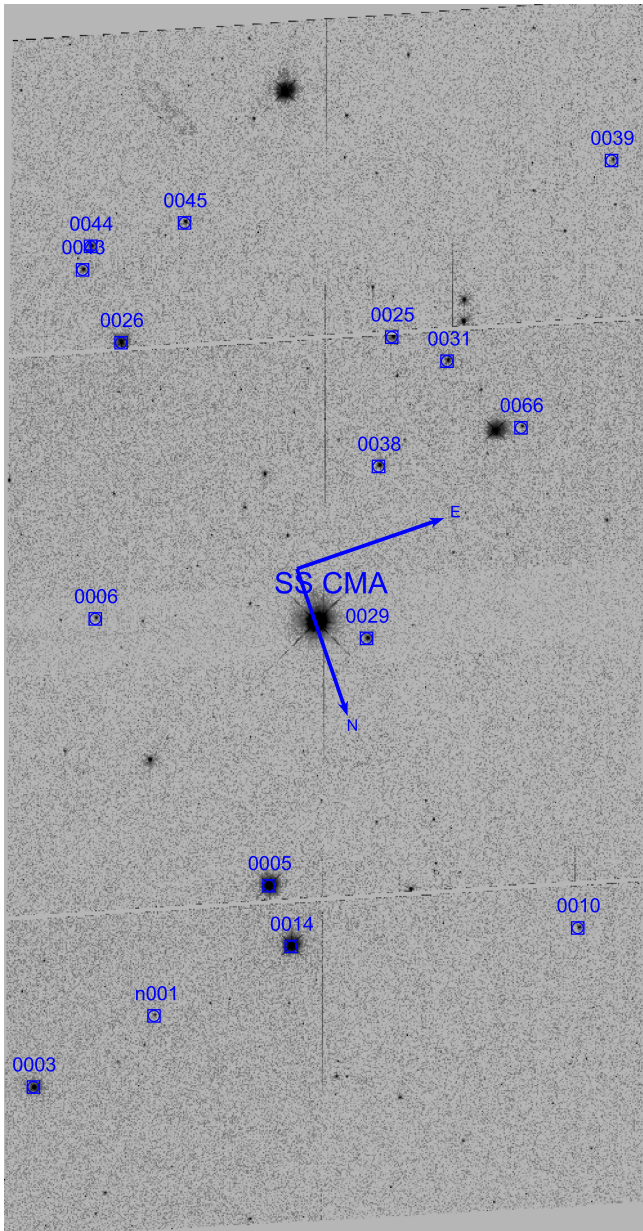


Figure 1. *HST* WFC3–UVIS images ($2\rlap{.}^{\prime}7 \times 4\rlap{.}^{\prime}7$) of the field centered around Cepheid SS CMA covered by WFC3–UVIS spatial scanning. Compass indicates directions of north and east. Spectrophotometric reference stars are labeled.

includes the aperture correction of the scanned data LSF from its 15 pixel minirow extent to an infinite aperture as used for imaging data. In addition, measuring this empirically would include and thus cancel an error in the combination of the pixel size and scan rate (used to define the effective exposure time), as these same values are used for the reference-star scans. The same programs (GO-13335, GO-13928) used to obtain additional Cepheid scans also obtained staring mode images and contain additional reference stars in a useful magnitude range. In F160W, there were 88 observations of stars in the fields of the Cepheids in a useful magnitude range of $12.5 < F160W < 14.0$. The difference between the scanned and staring photometry in F160W has a dispersion of 0.03 mag, primarily from staring mode errors due to undersampling and flat-field variation, and the offset has an error in the mean of 0.0033 mag. The same comparison at a much slower speed

($0\rlap{.}^{\prime}31 \text{ s}^{-1}$ instead of $7\rlap{.}^{\prime}5 \text{ s}^{-1}$) for 10 stars in M35 yields a consistent result (GO-13101). In F555W and F814W, 17 stars in M67 (GO-14394) in the range 11–15 mag were scanned ($0\rlap{.}^{\prime}40 \text{ s}^{-1}$) and imaged, and used to derive a constant offset between the scanning and staring mode apertures with a precision of 0.003 and 0.002 mag, respectively. This was successfully tested against 11 stars in the frames of the Cepheids at the higher scan speed.

When using Cepheid magnitudes to measure distances, it is useful to make use of a “phase correction,” the difference between the Cepheid magnitude at the observed phase and at the (flux) mean of their light curve, since the magnitude (at the time of mean flux) is the best distance indicator for Cepheids. These phase corrections are most efficiently derived from ground-based light curves of these Cepheids in matching filters. Because the phase corrections are relative quantities, they do not change the zeropoint of the light curves, which remain on the *HST* WFC3 natural system. The phase-correction uncertainties are determined from the variations around a locally smooth curve. The algorithm for determining the phase corrections and the sources of the ground-based data are given in the Appendix.

The ground-based Cepheid light curves are shown in the Appendix together with the *HST* photometry. In F555W and F814W each Cepheid was observed at 3–5 epochs. In F160W, each was observed at 3–6 epochs.

With photometry of this precision, the use of individual epochs to calibrate the luminosity of Cepheids is dominated by the uncertainties in the phase corrections. The mean uncertainties in these phase corrections per epoch are 0.035, 0.023, and 0.018 mag in F555W, F814W, and F160W (respectively). The phase-correction errors scale with the size of magnitude changes in the light curves and are thus smallest in the NIR. These values are consistent with the dispersion of multiple epochs measured for the *HST* observations around the ground-based light curves. The mean uncertainty in the light-curve mean magnitude for these seven Cepheids is 0.021, 0.010, and 0.009 mag in F555W, F814W, and F160W, respectively. At this level of precision, parallax uncertainties will dominate the determination of absolute luminosities for uncertainties greater than $5 \mu\text{as}$.

In Table 4, we provide the photometric measurements of these seven Cepheids for WFC3 F555W, F814W, and F160W.

4. A Test of the Calibration of the Hubble Constant

Here we seek to test the Cepheid calibration of the Hubble constant. However, for simplicity, we will initially avoid contending with the well-known bias that arises in the conversion of parallax measurements with modest S/N to absolute magnitudes, often referred to as the Lutz–Kelker–Hanson bias (LKH; Hanson 1979). Because the uncertainty in the parallaxes we would predict for these Cepheids based on their periods and magnitudes is a factor of 15–20 smaller than their measured parallax uncertainties, we compare the unbiased parallax predictions (expected bias < 0.001 mag) directly to the measurements. Carrying out this fit in parallax space avoids nonlinear transformations of the relatively large parallax error. A similar method has been used, e.g., by Feast & Catchpole (1997) in their luminosity calibration of Cepheids from *Hipparcos* parallaxes; see Sesar et al. (2017) for a recent detailed discussion. We will make use of the measured parallaxes to determine absolute magnitudes and account for the LKH bias in Section 4.1.

Table 2
Reference Stars

Star	R.A.	Decl. (deg)	Class	Quality	Source	T_{eff}	σ	$\log g$	σ	$F606W$	μ (mag)	σ
sscma0003	111.4971	-25.2325	K0IV	fair	Gemini	5340	156	3.74	0.5	13.85	11.66	0.10
sscma0005	111.5198	-25.2406	A7V	good	Gemini	7920	254	3.89	0.5	12.34	9.779	0.11
sscma0006	111.5137	-25.2626	G5IV	vgood	N/A	5730	114	3.80	0.5	16.56	10.80	0.13
sscma0010	111.5417	-25.2306	F7IV	vgood	Gemini	6550	205	3.89	0.5	16.33	11.33	0.13
sscma0014	111.5199	-25.2360	F5IV-V	vgood	Lick	6700	134	3.96	0.5	12.33	9.142	0.12
sscma0025	111.5430	-25.2747	G5IV-V	good	Lick	5730	114	3.89	0.5	14.72	10.72	0.14
sscma0026	111.5227	-25.2806	A2III-IV	vgood	Lick	8675	362	4.44	0.5	13.71	11.57	0.14
sscma0029	111.5334	-25.2550	G6V	vgood	Gemini	5693	133	4.24	0.5	15.33	10.16	0.11
sscma0031	111.5465	-25.2718	F8IV	vgood	Gemini	6425	156	3.88	0.5	15.46	11.07	0.14
sscma0038	111.5387	-25.2663	G0V	vgood	Lick	5745	328	4.23	0.5	15.55	11.14	0.11
sscma0039	111.5639	-25.2815	G0V	fair	Lick	6300	180	4.12	0.5	16.69	11.34	0.15
sscma0043	111.5217	-25.2864	K5III	good	Keck	5500	188	1.00	0.1	15.26	17.67	0.15
sscma0044	111.5229	-25.2878	G2IV-V	good	Lick	5800	185	3.90	0.5	15.33	10.88	0.10
sscma0045	111.5305	-25.2872	F8II-III	fair	Lick	6300	128	3.20	0.6	15.58	13.09	0.10
sscma0066	111.5503	-25.2656	G6IV-V	good	Lick	5513	133	3.86	0.5	17.08	11.89	0.65
sscman001	111.5079	-25.2345	NA	NA	NA	0	0	0.00	0.0	0.000	11.10	0.17
xycar0065	165.5151	-64.2920	M5III	poor	Gemini	5440	133	0.00	0.0	16.59	13.85	0.10
xycar0068	165.6194	-64.2607	F8IV-V	good	Gemini	6300	156	3.94	0.5	15.99	11.23	0.15
xycar0071	165.6018	-64.2744	G9IV	vgood	Gemini	5390	156	3.75	0.5	15.81	11.80	0.25
xycar0083	165.5281	-64.2914	K4	fair	Gemini	4600	260	0.00	0.0	15.44	13.10	0.15
xycar0098	165.5259	-64.2498	F8V	vgood	Gemini	6425	156	4.10	0.5	14.75	10.36	0.15
xycar0100	165.5023	-64.2788	A1IV-V	vgood	Gemini	9185	339	3.94	0.5	14.67	11.75	0.10
xycar0105	165.5614	-64.2864	K4II	good	Gemini	5020	509	1.95	0.7	12.51	12.01	0.22
xycar0121	165.5442	-64.2957	M5III	poor	Gemini	5800	185	0.00	0.0	15.28	10.45	0.52
xycar0123	165.5456	-64.2951	G8IV	good	SOAR	5440	133	3.76	0.5	15.60	11.58	0.19
xycar0179	165.5647	-64.2606	A4IV	good	Gemini	8200	339	3.98	0.5	14.29	11.05	0.13
xycar0243	165.5724	-64.2306	A6IV	good	Gemini	8212	254	3.99	0.5	16.39	12.41	0.10
vxper0030	31.98145	58.42410	GOIV-V	good	Keck	5925	180	3.91	0.5	16.12	10.76	0.60
vxper0035	32.00800	58.42643	F4V	good	Lick	6662	134	4.06	0.5	15.47	11.01	0.14
vxper0036	31.90272	58.46210	kA6hA8mF2-	NA	Keck	7920	254	0.00	0.0	15.34	11.54	0.10
vxper0039	31.99930	58.43603	F1IV	vgood	Keck	7275	205	3.95	0.5	15.00	10.84	0.10
vxper0041	31.98719	58.45766	mA6V	NA	Lick	7730	248	0.00	0.0	14.61	11.39	0.12
vxper0042	31.91492	58.43107	F9IV-V	vgood	Keck	6237	180	3.93	0.5	14.11	9.639	0.20
vxper0043	31.92551	58.46995	G5V	vgood	Lick	5730	114	4.23	0.5	14.10	8.968	0.31
vxper0044	31.93525	58.46506	F8III	good	Hydra	6175	156	3.42	0.6	14.43	10.10	0.76
vxper0049	31.92722	58.43344	B1V	vgood	Keck	26100	1000	3.67	0.5	11.36	12.08	0.11
vxper0067	31.88844	58.44349	K5I	good	Lick	4600	260	0.97	0.7	11.77	12.09	0.18
vxpern001	31.93254	58.46487	F5V	fair	Lick	6700	116	4.05	0.5	16.49	11.77	0.10
wzsgr0090	274.2439	-19.0481	G5II	fair	Keck	5230	153	2.13	0.7	15.40	12.97	0.10
wzsgr0109	274.2284	-19.0566	K0III-IV	fair	Lick	4920	156	2.88	0.7	14.45	12.88	0.10
wzsgr0119	274.2306	-19.0513	G9II	fair	Lick	5390	156	2.27	0.7	14.39	12.77	0.10
wzsgr0120	274.2613	-19.0543	K4III	good	Lick	4600	188	2.42	0.7	14.04	11.62	0.11
wzsgr0122	274.2547	-19.0919	G7IV-V	vgood	Lick	5656	133	3.88	0.5	14.75	9.446	0.37
wzsgr0124	274.2527	-19.0568	F9V	vgood	Lick	6237	180	4.13	0.5	14.00	9.609	0.12
wzsgr0162	274.2926	-19.0923	F8V	good	Lick	6425	156	4.10	0.5	15.55	11.40	0.13
wzsgr0191	274.2534	-19.0908	G9V	fair	Lick	5070	156	4.39	0.5	16.36	12.08	0.10
wzsgr0269	274.2708	-19.0476	K0III-IV	good	Lick	5340	156	3.25	0.6	13.53	11.75	0.13
wzsgr0275	274.2674	-19.0473	NA	NA	NA	0	0	0.00	0.0	16.01	11.97	0.11
wzsgr0306	274.2657	-19.0323	G3V	good	Lick	6026	153	4.17	0.5	16.81	11.18	0.12
wzsgr0310	274.2623	-19.0389	F4III	fair	Lick	7347	212	3.79	0.5	15.66	11.29	0.12
wzsgrn003	274.2803	-19.0822	NA	NA	NA	0	0	0.00	0.0	12.67	11.11	0.28
svl0008	297.1140	27.30387	G6II	good	Lick	5513	133	2.38	0.7	13.81	13.01	0.10
svl0015	297.0976	27.31197	F0V	good	Lick	7635	248	3.93	0.5	14.78	11.72	0.19
svl0016	297.0758	27.28951	G7III	fair	Lick	5156	208	2.87	0.7	15.13	12.86	0.13
svl0019	297.1244	27.28699	F6V	good	Lick	6550	205	4.08	0.5	15.21	11.15	0.32
svl0020	297.1009	27.26104	K6-	good	Keck	5440	133	0.00	0.0	15.70	14.17	0.10
svl0021	297.0982	27.27661	G1V	fair	Lick	5865	175	4.20	0.5	15.71	10.39	0.49
svl0028	297.1217	27.28104	F2II	good	Lick	7200	205	4.03	0.5	16.08	13.03	0.10
svl0041	297.1052	27.29179	F1V	good	Keck	7275	205	3.97	0.5	15.83	12.86	0.11
svl0042	297.1041	27.24918	G7III-IV	good	Keck	5476	133	3.35	0.6	16.21	13.32	0.10
svl0062	297.0741	27.31131	G9IV	good	Keck	5390	156	3.75	0.5	16.68	13.19	0.11

Table 2
(Continued)

Star	R.A.	Decl. (deg)	Class	Quality	Source	T_{eff}	σ	$\log g$	σ	$F606W$	μ (mag)	σ
svul0074	297.1284	27.28546	F5Ia	fair	Lick	7310	212	1.88	0.7	17.01	13.14	0.10
svuln009	297.0882	27.31561	K6–	poor	Lick	5440	133	0.00	0.0	16.89	14.17	0.10
svuln016	297.0818	27.29010	G8III	good	Lick	5440	133	3.05	0.6	15.63	13.39	0.10
xpup0004	113.1950	−20.9228	B7V	fair	Keck	13500	647	3.59	0.5	12.87	12.88	0.10
xpup0008	113.1849	−20.8820	NA	NA	NA	5440	133	0.00	0.0	14.43	13.03	0.10
xpup0011	113.2106	−20.9232	F2V	vgood	Hydra	7200	205	3.98	0.5	14.96	11.38	0.10
xpup0014	113.2090	−20.8689	F5V	good	Lick	6875	134	4.03	0.5	15.02	11.14	0.11
xpup0017	113.2245	−20.9229	A0V	vgood	Hydra	9600	1000	3.75	0.5	15.04	12.11	0.15
xpup0021	113.2240	−20.8950	F8V	vgood	Keck	6300	156	4.12	0.5	15.63	11.16	0.11
xpup0027	113.2173	−20.8660	F7V	vgood	Lick	6350	205	4.11	0.5	0.000	11.22	0.12
xpup0028	113.1836	−20.8876	F4V	good	Keck	7907	212	3.89	0.5	16.00	11.91	0.10
xpup0032	113.2124	−20.8985	F9IV	good	Keck	6362	180	3.88	0.5	16.40	11.65	0.12
xpup0036	113.2067	−20.8719	F1V	good	Keck	7125	205	3.99	0.5	16.58	12.28	0.10
xpup0044	113.2284	−20.8957	F2IV-V	vgood	Keck	6800	205	3.96	0.5	16.90	12.19	0.12
xpup0048	113.2042	−20.8753	G9III-IV	good	Keck	5390	156	3.28	0.6	17.00	13.66	0.10
xpup0050	113.1978	−20.8819	G9V	good	Keck	5390	156	4.31	0.5	17.44	11.89	0.34
xpupn000	113.2137	−20.9025	NA	NA	NA	0	0	0.00	0.0	17.33	9.881	0.28
xpupn001	113.2109	−20.9313	NA	NA	NA	0	0	0.00	0.0	17.86	11.73	0.10
xpupn002	113.2162	−20.9311	NA	NA	NA	0	0	0.00	0.0	17.52	9.881	0.28
xpupn004	113.2137	−20.9025	NA	NA	NA	0	0	0.00	0.0	17.33	13.43	0.35
vycar0010	161.1465	−57.5821	F2V	good	AAT	7200	205	3.98	0.5	13.69	11.11	0.23
vycar0021	161.1578	−57.5941	A0V	vgood	Gemini	9600	1000	3.75	0.5	14.74	12.30	0.17
vycar0029	161.0890	−57.5733	G0V	good	N/A	6175	180	4.14	0.5	15.77	11.09	0.16
vycar0051	161.1569	−57.5693	G9IV-V	vgood	Gemini	5390	156	3.85	0.5	13.39	8.944	5.49
vycar0060	161.1321	−57.5448	mAV4	NA	SOAR	7920	254	0.00	0.0	12.72	10.35	0.26
vycar0077	161.1772	−57.5360	K5III-IV	vgood	N/A	4680	260	2.64	0.7	15.10	13.31	0.10
vycar0078	161.1733	−57.5367	F1III-IV	vgood	Gemini	7275	205	4.19	0.5	14.90	11.36	0.12
vycar0091	161.1576	−57.5454	F1III-IV	good	Gemini	7275	205	4.19	0.5	15.86	12.11	0.19
vycar0109	161.1333	−57.5529	F0V	vgood	Gemini	7350	248	3.96	0.5	15.80	12.13	0.12
vycar0124	161.1082	−57.5855	F4IV-V	good	Gemini	7062	134	3.97	0.5	15.40	12.72	0.12
vycar0129	161.1388	−57.5943	KA1hA7mA9–	NA	Gemini	7920	254	0.00	0.0	14.80	12.23	0.13
vycar0147	161.0889	−57.5815	F5IV-V	vgood	AAT	6875	134	3.97	0.5	13.46	10.26	0.43
vycar0148	161.1004	−57.5866	NA	NA	NA	7920	254	0.00	0.0	16.98	13.18	0.10
vycar0150	161.0962	−57.5918	A7	fair	Gemini	6300	156	0.00	0.0	16.50	11.79	0.11
vycar0153	161.0987	−57.5874	F0	fair	Gemini	6300	156	0.00	0.0	17.26	12.51	0.12
vycar0179	161.0943	−57.5729	K3V	good	Gemini	5120	412	4.38	0.5	16.22	9.762	0.15
vycar0226	161.1098	−57.5324	K3III	vgood	AAT	5120	412	2.84	0.7	11.91	11.12	0.43
vycar0231	161.1043	−57.5396	NA	NA	NA	0	0	0.00	0.0	13.41	11.63	0.20

Using the known periods of these Cepheids and their photometry in Table 4, we can predict their parallaxes using the distance-ladder parameters presented by Riess et al. (2016) as in Casertano et al. (2017). This is equivalent to reversing the distance ladder to predict the parallaxes from H_0 . First, we form the same Wesenheit reddening-free magnitudes used by R16 (Madore 1982):

$$m_H^W = m_{F160W} - 0.386(m_{F555W} - m_{F814W}). \quad (1)$$

These m_H^W values have a mean uncertainty of 0.012 mag.

There is a small count-rate nonlinearity effect (hereafter CRNL) that can make faint sources appear too faint in HgCdTe devices like WFC3-IR due to charge trapping. This term has been measured to be 0.008 ± 0.003 mag dex $^{-1}$ for WFC3-IR (Riess 2011, A. Riess 2018, in preparation). We correct for the CRNL by adding 0.026 ± 0.009 mag to account for the 3.2 dex between the observed count rates of MW Cepheids and the extragalactic Cepheids of Riess et al. (2016).

The best-fit solution from Riess et al. (2016) yields a value of H_0 of $H_0 = 73.24 \text{ km s}^{-1} \text{ Mpc}^{-1}$. Based on this value, the derived calibration of the Cepheid P - L relation is

$$M_H^W = -5.93 - 3.26(\log P - 1). \quad (2)$$

Employing the derived periods (see the Appendix) yields the values of M_H^W , and combined with the apparent Wesenheit magnitudes on the WFC3 system (m_H^W) we derive distance moduli of

$$\mu = m_H^W - M_H^W \quad (3)$$

and the expected parallax

$$\pi_{\text{R16}} = 10^{-0.2(\mu-10)} \quad (4)$$

in mas. With negligible uncertainties in the periods, the mean uncertainties in the predicted μ are 0.015 mag, or <1% in distance. These expected parallaxes on the scale in which $H_0 = 73.24 \text{ km s}^{-1} \text{ Mpc}^{-1}$ are given in Table 4 as π_{R16} .

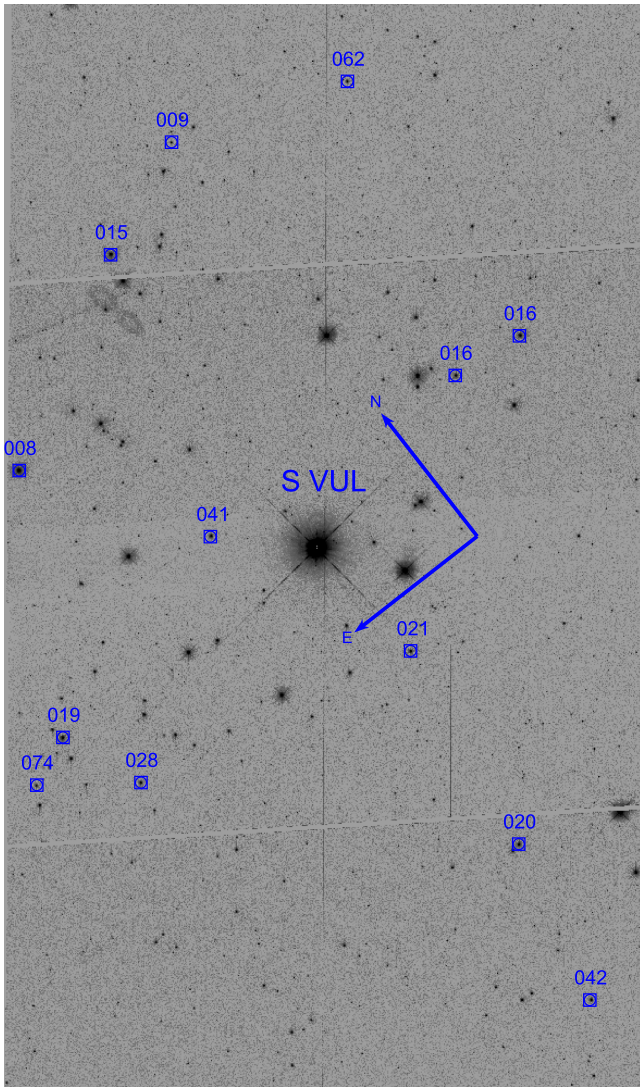


Figure 2. Same as Figure 1, but for S Vul.

(These are weakly correlated owing to the CRNL correction uncertainty of 0.009 mag, but this is insignificant compared to the measured uncertainties in the parallaxes.)

In Figure 10, we compare the predicted and measured parallaxes for the eight Cepheids from this program (seven presented here and SY Aur from Paper I: measured = 0.428 ± 0.054 mas, predicted = 0.418 mas). The agreement between the measured and predicted parallaxes is reasonably good: total $\chi^2 = 12.9$ for eight points, with a higher value expected to occur 15% of the time by chance.

Now we can consider whether there is a better scale for the predicted parallaxes—that is, a preferred value of H_0 that improves the agreement with the measured parallaxes. Such a value of α would favor a new value of H_0 from an independent calibration of the Cepheids as $H_{0,\text{new}} = \alpha (H_{0,\text{R16}})$. To determine this, we minimize the usual χ^2 statistic for the set of eight parallaxes,

$$\chi^2 = \sum \frac{\alpha \pi_{\text{R16}} - \pi_{\text{obs}}}{\sigma}, \quad (5)$$

with respect to a free parameter (α) used to vary the distance scale of R16, that is $\pi_{\text{obs}} = \alpha \pi_{\text{R16}}$. We find a value of

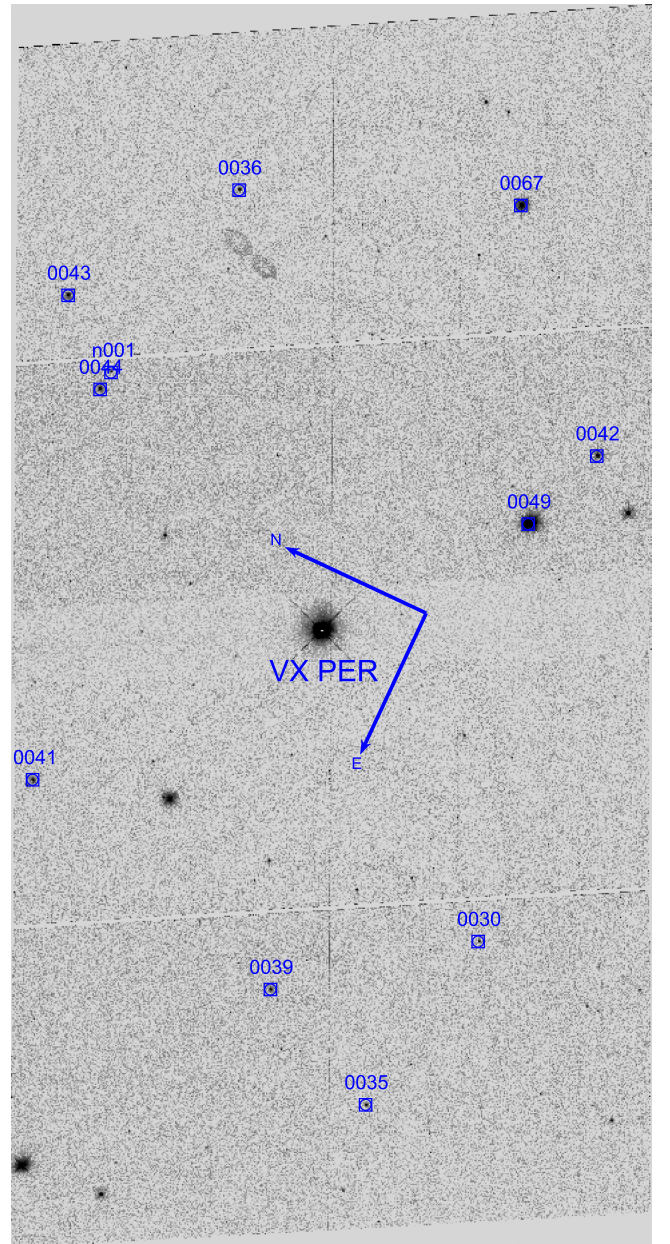


Figure 3. Same as Figure 1, but for VX Per.

$\alpha = 1.037 \pm 0.036$ (with the best $\chi^2 = 11.9$), as shown in Figure 11, consistent with no rescaling.

Reducing the predicted parallaxes by 9%, equivalent to increasing their mean μ by 0.20 mag ($\alpha = 0.91$) to place them on the $H_0 = 67 \text{ km s}^{-1} \text{ Mpc}^{-1}$ scale of Planck (Planck Collaboration et al. 2016) and Λ CDM, results in a total $\chi^2 = 24.2$, or an increase of 12.3 for one degree of freedom, a result disfavored at the 3.5σ (99.9%) confidence level. This result is independent of the use of the masers in NGC 4258, the DEBs in the LMC, and the parallaxes of MW Cepheids measured with the HST FGS from Benedict et al. (2007) and augmented by Hipparcos (van Leeuwen et al. 2007), used by R16 to determine H_0 .

4.1. The MW Cepheid P–L Relation and H_0

Use of the measured Cepheid parallaxes with modest S/N and their apparent magnitudes to estimate their absolute

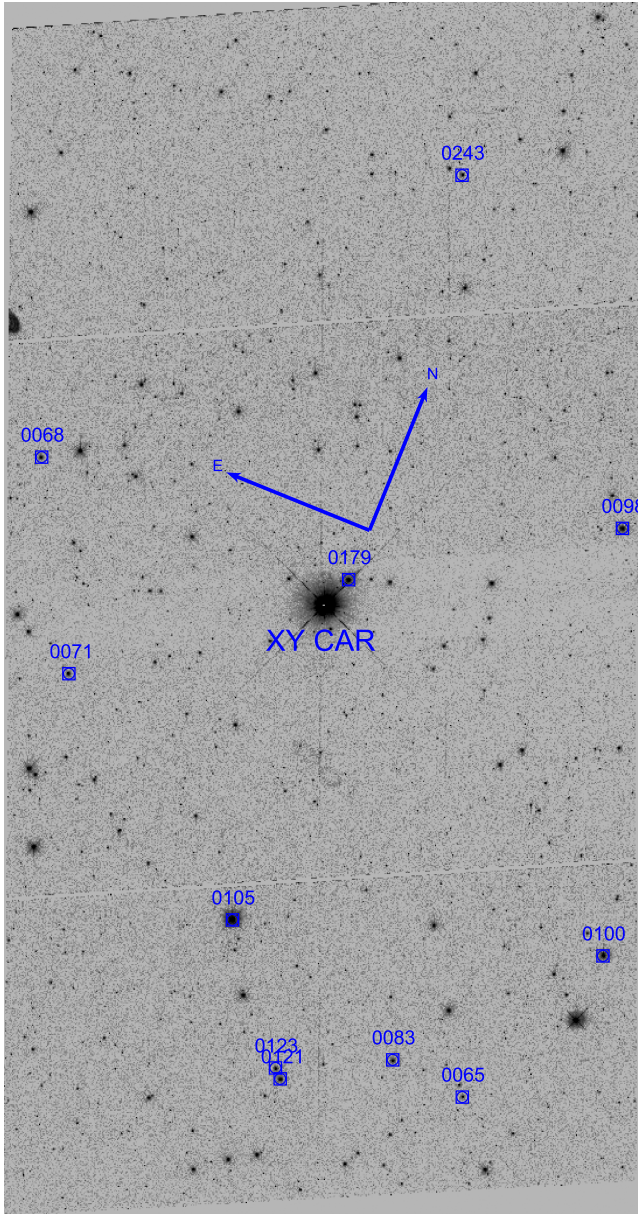


Figure 4. Same as Figure 1, but for XY Car.

magnitudes requires a small correction for the LKH bias, which we estimate following Benedict et al. (2007) and van Leeuwen et al. (2007; Table 4).¹⁰

This bias may be considered in two parts: (a) the change in shape of the PDF of the parallax estimate when used to estimate its inverse, i.e., $D = \pi^{-1}$ or $\mu = 5 \log D + 10$, and (b) the nonuniformity of the a priori distribution of possible distances (and ultimately magnitudes) for a disk population of stars with a given measured parallax, i.e., there are more stars with $D = \pi^{-1} + \sigma$ consistent with a parallax measurement than those with $D = \pi^{-1} - \sigma$. For each parallax measurement, we use the density distribution used by the Besançon Model of the Galaxy (Robin et al. 2003) for young (<1 Gyr) stars to produce a realistic distribution of stars along each line of sight. We then average their magnitudes weighted by their

¹⁰ This bias does not apply when comparing different measurements of the parallax for the same object and is negligible for the conversion of high-S/N measurements of magnitudes to parallax.

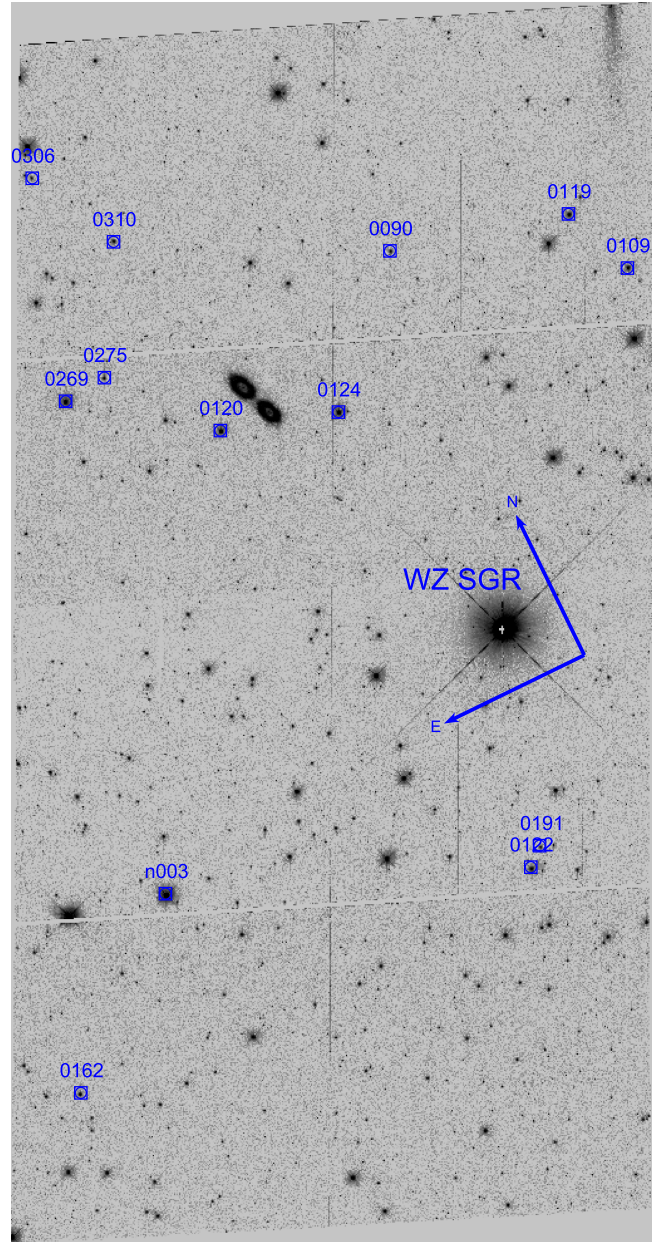


Figure 5. Same as Figure 1, but for WZ Sgr.

consistency with the parallax measurement and derive the LKH bias as the difference of this average with the value derived from the nominal measured parallax. Our estimates of the LKH bias match those of van Leeuwen et al. (2007), with a mean difference of <0.001 mag and an individual dispersion of 0.02 mag, and are listed for the new parallaxes in Table 4.

The debiased distance modulus is then given by

$$\mu = 5 \log \pi_{\text{obs}}^{-1} + 10 - \text{LKH} \quad (6)$$

and the absolute magnitude is derived from μ and the flux (see Equations (1) and (3)). The absolute P - L relation in the WFC3 Wesenheit system for these eight MW Cepheids is shown in Figure 12 together with the results from Benedict et al. (2007) and van Leeuwen et al. (2007). The new set is consistent with the prior measurements, but it now usefully extends the well-sampled range to $P > 10$ days, while avoiding the uncertainties

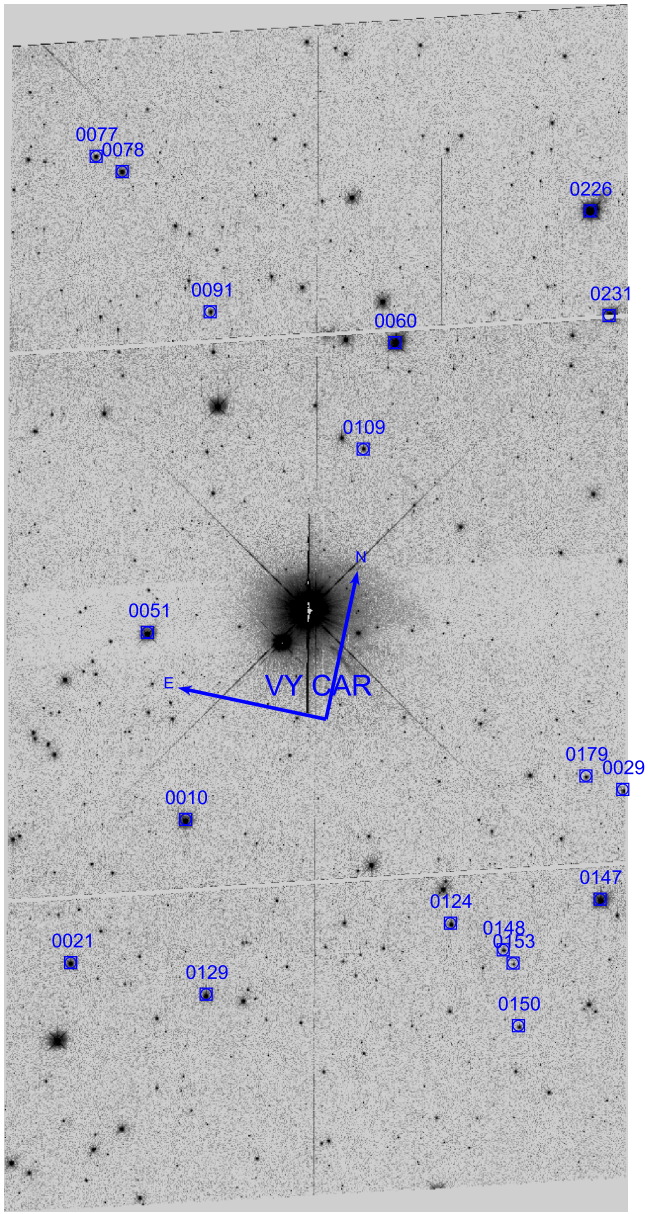


Figure 6. Same as Figure 1, but for VY Car.

in transforming from ground-based to the WFC3 photometric system.

Following R16, we can utilize this expanded P - L relation to help calibrate the luminosity of SNe Ia and improve the determination of the value of H_0 . Of the three geometric sources of Cepheid luminosity calibration used by R16 to determine H_0 (masers in NGC 4258, DEBs in the LMC, and MW Cepheid parallaxes), the MW Cepheids yielded the highest value of $76.2 \pm 2.4 \text{ km s}^{-1} \text{ Mpc}^{-1}$, which is 1.5σ higher than the mean of the other two, $71.6 \pm 1.8 \text{ km s}^{-1} \text{ Mpc}^{-1}$. It is not uncommon for the highest measurement among three to differ at this level from the mean of the lower two (probability of 17%). As noted in the previous section, the new parallax measurements modestly decrease the inferred value of H_0 when used with the prior MW Cepheid parallaxes and yields $75.9 \pm 2.1 \text{ km s}^{-1} \text{ Mpc}^{-1}$. Including the new parallax measurements with all three anchors yields $H_0 = 73.48 \pm 1.66 \text{ km s}^{-1} \text{ Mpc}^{-1}$, a reduction in total error (including systematics) from 2.37% to 2.27%. There is a

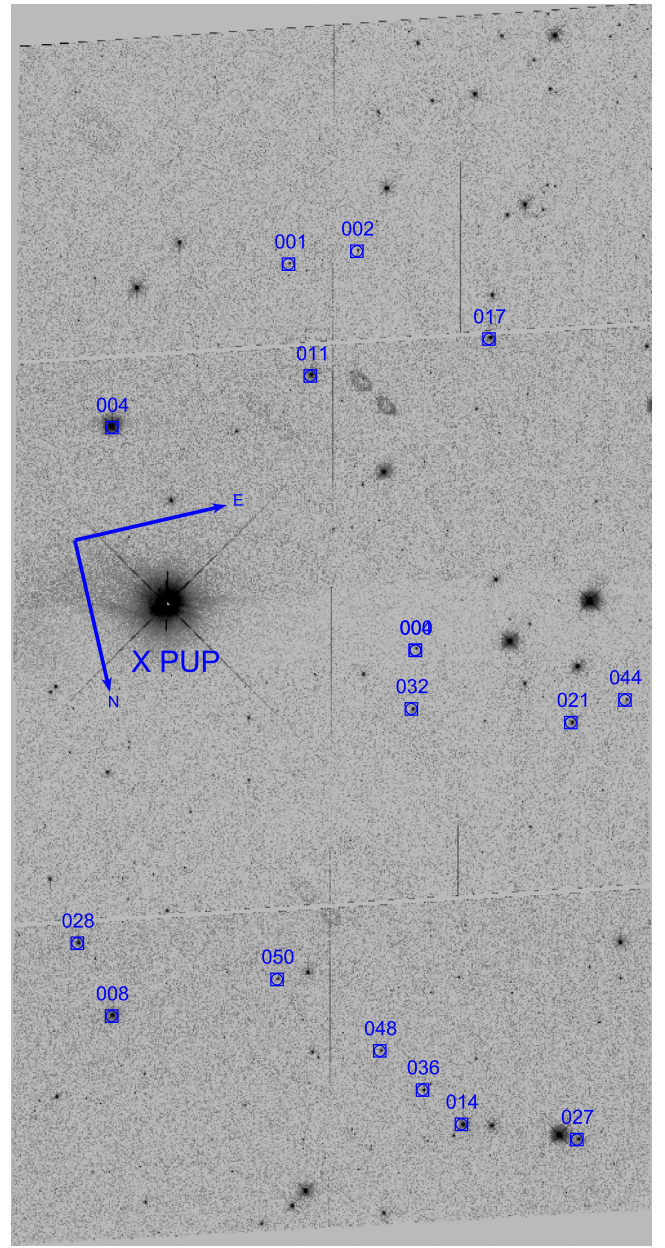


Figure 7. Same as Figure 1, but for X Pup.

small increase in H_0 of $0.24 \text{ km s}^{-1} \text{ Mpc}^{-1}$ from the R16 value owing to a small covariance between the parameters and measurements of the other two anchors. Comparing the difference between this locally determined value of H_0 and the value from *Planck* and Λ CDM (Planck Collaboration et al. 2016) increases the significance of the difference from 3.4σ seen by R16 to now 3.7σ .

5. Discussion

The eight MW Cepheid parallax and photometric measurements presented here provide an alternative source to calibrate the Cepheid P - L relation with two advantages over the prior MW sample: (1) their periods, with a range of $10 < P < 69$ days and a mean of 18 days, provide a better match to the $P > 10$ day extragalactic Cepheids detectable in SN Ia host galaxies, and (2) they use the same WFC3 photometric system

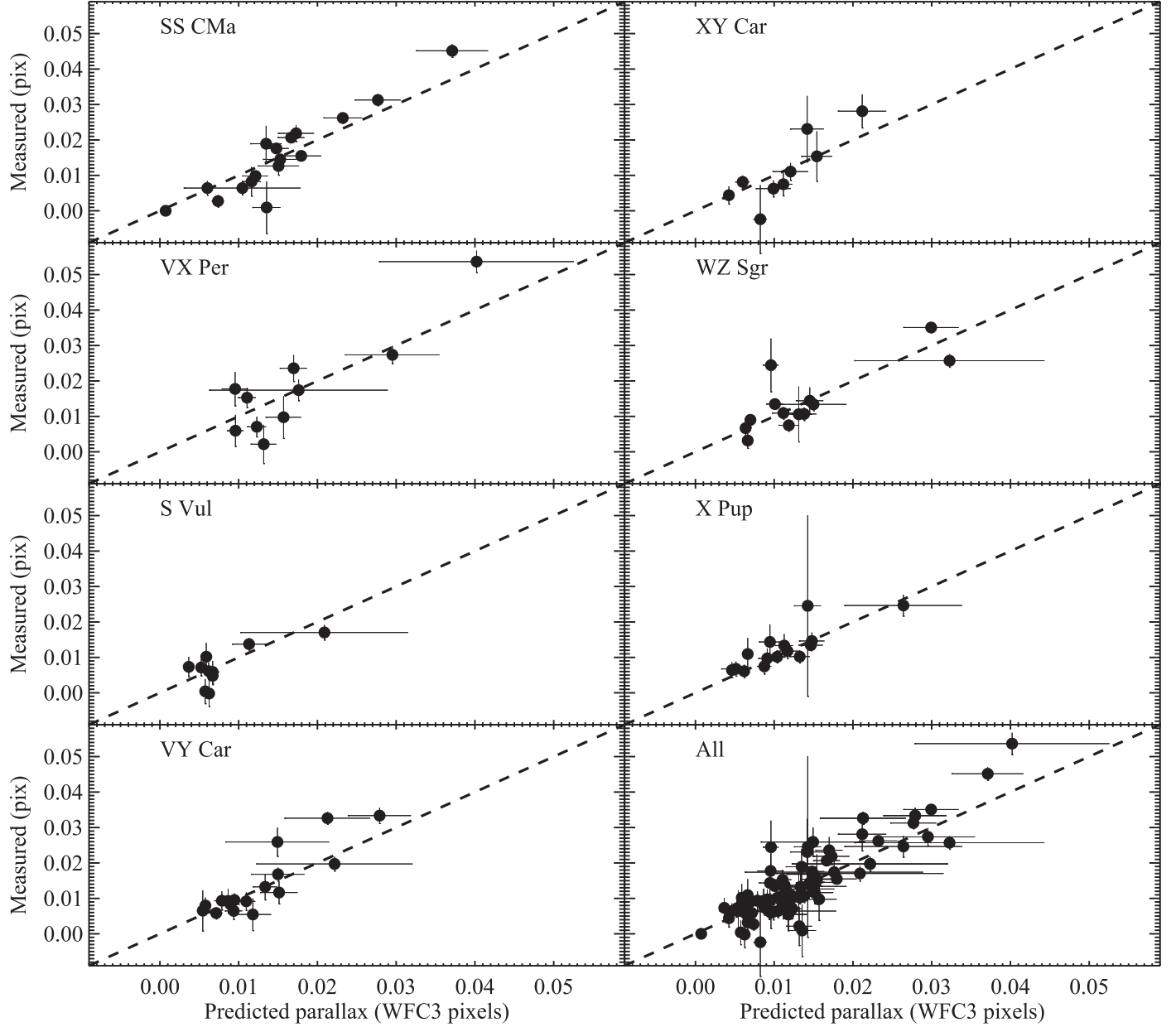


Figure 8. Comparison between spectrophotometric and pure astrometric parallax, obtained by excluding the spectrophotometric prior for each star in turn. In this comparison, the astrometric parallax is fully independent of the spectrophotometric parallax.

as these extragalactic Cepheids. As previously seen with all three anchors used by R16, the new data confirm the tension seen with Planck Collaboration et al. (2016) used in conjunction with Λ CDM to predict the value of H_0 .¹¹ With now four independent sources of calibration, it is very hard to imagine that systematic errors in the calibration of the distance ladder are the root cause of the tension. As discussed in Section 1, neither a replacement of the Cepheids as the bridge to SNe Ia nor of the SN Ia optical magnitudes produces a meaningful shift in the local determination of the Hubble constant. Elsewhere, it has been shown that variations between

the local and global value of H_0 are expected and observed to be $\sim 0.3\%$ (Odderskov et al. 2014, 2017; Riess et al. 2016; Wu & Huterer 2017), a factor of 30 smaller than the present 9% difference.

Additional precision in the calibration of the distance ladder is expected from forthcoming releases of the ESA *Gaia* mission. Already Data Release 1 (DR1) provided hundreds of Cepheid parallax measurements. Although the DR1 parallaxes had an order of magnitude less precision than those presented here (see Figure 10), they are more numerous, and the precision by the expected final data release in ~ 2022 is expected to be a factor of 4–5 better than what we have achieved with the WFC3 scanning approach. While it is not yet clear if one can reasonably combine hundreds of low-S/N measurements of DR1 Cepheid to produce one high-S/N measurement without penalty, Casertano et al. (2017) showed that the result of doing so was a scale of $\alpha = 0.997 \pm 0.031$, consistent with the result

¹¹ Anderson & Riess (2017) have estimated a small bias (0.2%) in the value of H_0 owing to the association of Cepheids with clusters and the changing resolution along the distance ladder. Correcting for this association bias would decrease H_0 to $73.27 \text{ km s}^{-1} \text{ Mpc}^{-1}$ and lower the tension with *Planck* from 3.7σ to 3.6σ .

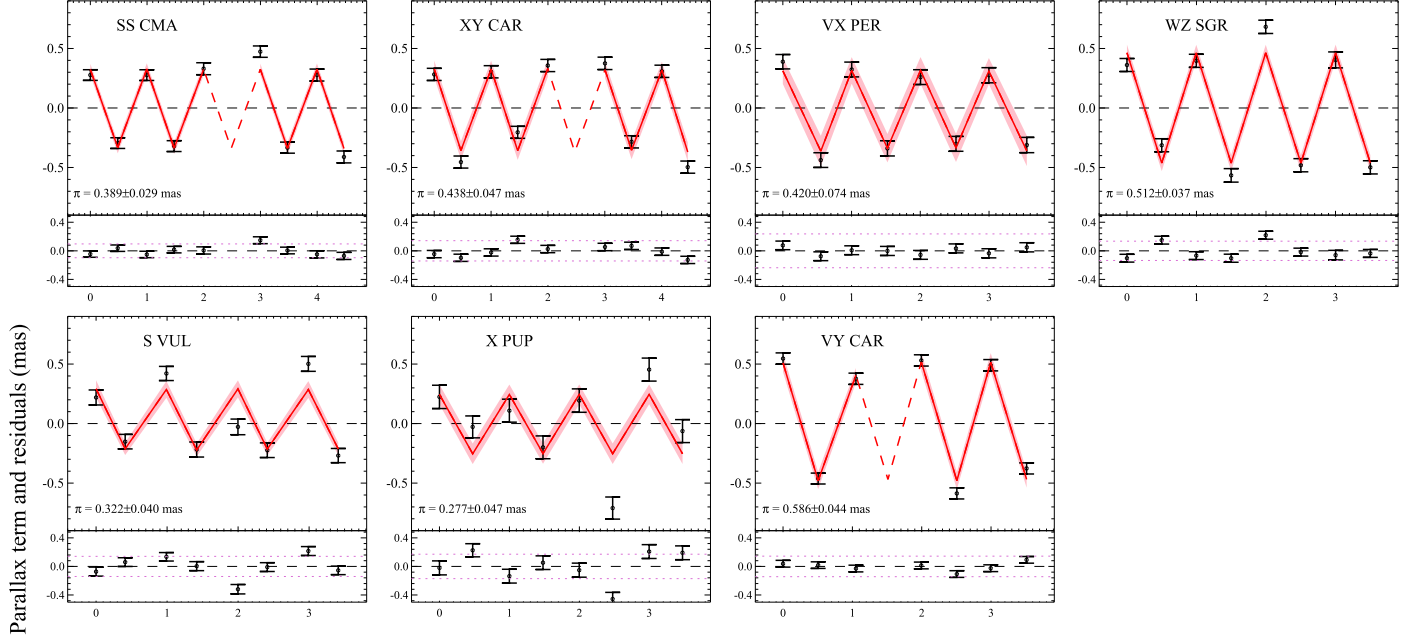


Figure 9. Proper-motion-subtracted 1D motion of the Cepheids observed at 6 month epochs spaced over 4 years. The red line indicates the best model fit of the parallax motion. Plotted values include the parallax factor.

Table 3
Parallax

Cepheid	π (milliarcsec)	σ_{tot}	σ_{abs}
SS CMa	0.389	0.0287	0.003
XY Car	0.438	0.0469	0.011
VX Per	0.420	0.0744	0.017
VY Car	0.586	0.0438	0.009
WZ Sgr	0.512	0.0373	0.011
S Vul	0.322	0.0396	0.007
X Pup	0.277	0.0469	0.009

Note. σ_{abs} is the contribution to σ_{tot} from the reduction from relative to absolute parallax.

of 1.037 ± 0.036 from the set of eight independent parallaxes presented here.

To make optimal use of the parallaxes from *Gaia*, with individual uncertainties expected to reach $\sim 3\%$ for hundreds of Cepheids, it is even more important to measure their photometry on the same *HST* WFC3 system as their extragalactic cousins. Failure to do so would leave the system-to-system systematic uncertainty in the NIR of $\sigma \sim 0.03$ mag (Skrutskie et al. 2006; Kalirai et al. 2009), precluding a 1% determination of H_0 . The match between the ground-based *H*-band and the WFC3 *F160W* is particularly poor as indicated by the large color term of ~ 0.2 mag per mag of $J - H$ color, which has been measured between the two (Riess 2011a; Riess et al. 2016).

To enable this goal, we have collected *F555W*, *F814W*, and *F160W* photometry of 50 of the most useful MW Cepheids ($P > 10$ days, lowest extinction, nearest, brightnesses suitable for *Gaia*) using the same approach as in Section 3. The expected error for this sample of 50 would be under 0.4% each for their mean parallax from *Gaia* and photometry from *HST*, and would keep the total uncertainty in H_0 to under 0.6%, a suitable anchor for a 1% determination of H_0 . Assuming

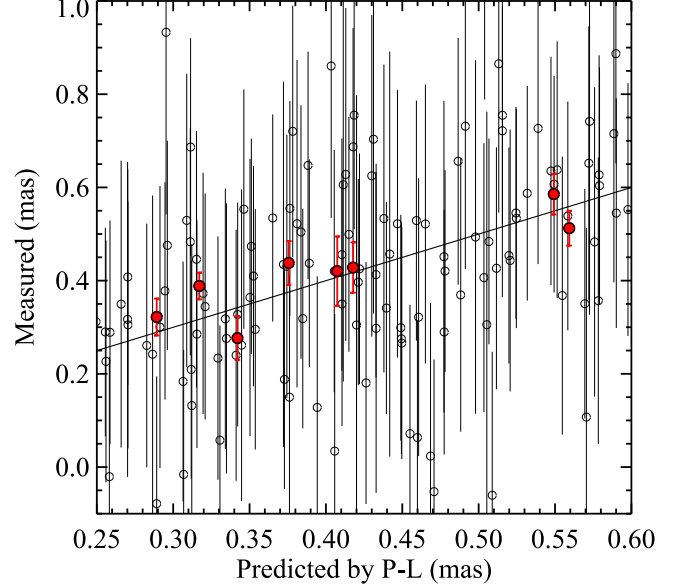


Figure 10. Comparison of predicted and measured parallaxes. The predictions are based on their Wesenheit apparent magnitudes and periods as well as the Cepheid *P-L* calibrated in R16, which yields $H_0 = 73.2 \text{ km s}^{-1} \text{ Mpc}^{-1}$. The eight points in red are from the spatial scanning program presented here. The open symbols are based on *Gaia* DR1.

comparable improvement in the tie between Cepheids and SNe Ia (50–60 systems), a measurement with this precision would match the precision of the CMB-based prediction and provide a powerful end-to-end test of the cosmological model.

This project was enabled by significant assistance from a wide variety of sources. Gautam Upadhyा, Aviv R. Cukierman, Merle Reinhardt, George Chapman, William Januszewski, and Ken Sembach provided help with the *HST* observations. We thank Ryan Foley and Yen-Chen Pan for obtaining spectra of two reference stars with SOAR and Peter

Table 4
Photometric Data for MW Cepheids

Cepheid	<i>F555W</i>	σ	std	eps	<i>F814W</i>	σ	std	eps	<i>F160W^a</i>	σ	std	eps	Period	π_{R16}	LKH
S VUL	9.138	0.028	0.050	3	6.856	0.010	0.017	3	4.885	0.009	0.026	4	68.966	0.289	-0.12
SS CMA	10.133	0.023	0.035	3	8.440	0.013	0.005	4	6.892	0.011	0.023	3	12.356	0.317	-0.03
VX PER	9.460	0.010	0.011	4	7.913	0.006	0.017	3	6.471	0.009	0.021	5	10.887	0.407	-0.10
VY CAR	7.591	0.029	0.102	5	6.224	0.008	0.040	5	4.972	0.007	0.031	6	18.898	0.549	-0.06
WZ SGR	8.177	0.016	0.027	5	6.476	0.012	0.034	5	4.856	0.010	0.046	4	21.851	0.559	-0.06
X PUP	8.692	0.026	0.016	3	7.129	0.010	0.015	3	5.626	0.008	0.020	4	25.967	0.342	-0.10
XY CAR	9.466	0.014	0.027	4	7.926	0.010	0.016	3	6.456	0.006	0.019	6	12.436	0.376	-0.07

Note.

^a Does not include the addition of 0.026 ± 0.009 mag to correct CRNL between MW and extragalactic Cepheids.

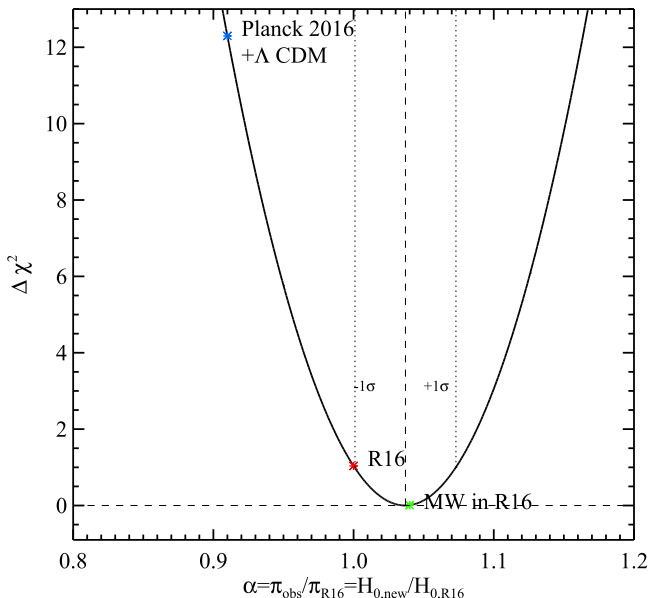


Figure 11. Change in χ^2 resulting from comparing the measured parallaxes of eight MW Cepheids to the values predicted by reversing the distance ladder (i.e., using the Hubble constant in R16), that is $\pi_{\text{obs}} = \alpha \pi_{\text{R16}}$ and $H_{0,\text{new}} = \alpha (H_{0,\text{R16}})$. Fractions less than unity indicate a lower Hubble constant. Position of the Planck 2016 + Λ CDM and the R16 result using only MW Cepheids as an anchor are indicated.

Challis for taking a few spectra of stars that were not ultimately used here. We thank Ed Nelan, Matt Lallo, Fritz Benedict, and Barbara McArthur for productive discussions about the behavior of the FGS. We also thank Leo Girardi, Alessandro Bressan, and Paola Marigo for the use of and assistance with their Padova isochrone database, Anne Robin for assistance with the Besancon Galaxy Model, Eddie Schlafly and D. Marshall for input on the extinction along the line of sight to these stars, and Nolan Walborn for useful discussions on the classification of hot stars. We thank Richard Anderson for useful discussions. We thank Scott Engle for observations relating to Cepheid period observations and Richard Gray for help with MK classification. We thank Kris Stanek for additional observations from the ASAS.

Support for this work was provided by the National Aeronautics and Space Administration (NASA) through programs GO-12879, 13334, 13335, 13344, 13571, 13678, 13686, 13928, 13929, 14062, 14394, 14648, and 14868 from the Space Telescope Science Institute (STScI), which is

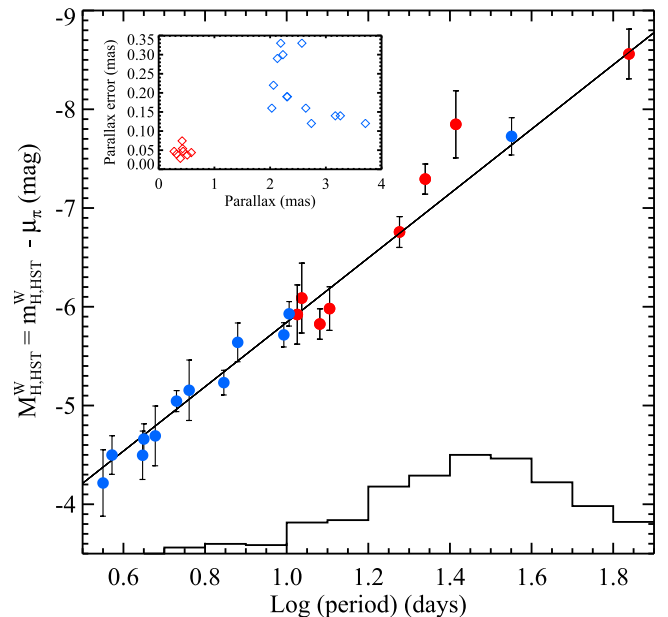


Figure 12. P – L relation of Milky Way Cepheids based on trigonometric parallax measurements. The points in blue were measured with the *HST* FGS (Benedict et al. 2007) and *Hipparcos* (van Leeuwen et al. 2007) and are all within 0.5 kpc, and the points in red are presented here from spatial scanning of WFC3 and are in the range of $1.7 < D < 3.6$ kpc. The inset shows the uncertainties in the measured parallaxes.

operated by AURA, Inc., under NASA contract NAS 5-26555. A.V.F.’s group at UC Berkeley is also grateful for financial assistance from NSF grant AST-1211916, the TABASGO Foundation, the Christopher R. Redlich Fund, and the Miller Institute for Basic Research in Science (UC Berkeley). S.C. and A.G.R. gratefully acknowledge support by the Munich Institute for Astro- and Particle Physics (MIAPP) of the DFG cluster of excellence “Origin and Structure of the Universe.” Research at Lick Observatory is partially supported by a generous gift from Google.

This research is based primarily on observations with the NASA/ESA *Hubble Space Telescope*, obtained at STScI, which is operated by AURA, Inc., under NASA contract NAS 5-26555. Some of the data presented herein were obtained at the W. M. Keck Observatory, which is operated as a scientific partnership among the California Institute of Technology, the University of California, and NASA; the Observatory was made possible by the generous financial support of the W. M.

Keck Foundation. This publication makes use of data products from the *Wide-field Infrared Survey Explorer (WISE)*, which is a joint project of the University of California (Los Angeles) and the Jet Propulsion Laboratory/California Institute of Technology, funded by NASA. It has also made use of the SIMBAD database, operated at CDS, Strasbourg, France.

Appendix

We made use of long-span multiband photometric measurements from the ground for each Cepheid in four bands (V , I , J , and H) to determine the phase corrections (the magnitude difference between an observed phase and the magnitude at the flux mean of the light curve) in the three similar WFC3 bands ($F555W$, $F814W$, and $F160W$).

We based our phase determination on seven data sets: (1) V -band measurements from the ASAS catalog of variable stars (Pojmanski 1997); (2) V -band measurements from the *INTEGRAL* Optical Monitoring Camera (Giménez et al. 2001); (3) multiband literature photometry measurements from the McMaster Cepheid Photometry and Radial Velocity Data Archive; (4) I -band measurements from Berdnikov et al. (2000); (5) JHK measurements from Monson & Pierce (2011); (6) our own H -band measurements using the CTIO 1.3 m telescope obtained in 2014–2015, and (7) V -band measurements from the 1.3 m RCT at Kitt Peak (S. Engle 2018, private communication). Data from different sources but with similar filters were merged to the same bands. For each band, we shifted light curves of various sources to a common zeropoint and rejected statistical outliers prior to the phase determination. The data used for each Cepheid are given in Table 5 and in Figure 13.

We fit the combined data set with Fourier series in order to create a model from which to estimate the phase correction. For each Cepheid, the combined measurements can be described by an $n \times 4$ matrix $\{t, m, \sigma, b\}$, where n is the number of measurements, t is the observation time, m is the magnitude, σ is the photometric uncertainty, and b is a band label. We ordered the data set by b and shifted t such that the midrange of the observation dates is zero. For each band, we construct a $n_b \times (2k_b + 1)$ matrix,

$$\begin{aligned} B_b = & \{1, \cos(\omega t_{bi}), \sin(\omega t_{bi}), \cos(2\omega t_{bi}), \\ & \sin(2\omega t_{bi}), \dots, \sin(k_b \omega t_{bi})\}, \\ i = & 1, 2, \dots, n_b, \end{aligned} \quad (7)$$

where n_b is the number of measurements in band b , t_{bi} is the time of the i th measurement in band b , k_b is the order of Fourier series for band b , and $\omega = 2\pi/P$ for a Cepheid with constant period P . Since the light-curve shapes can be different across different bands, while the Cepheid pulsating phase does not depend on wavelength, we construct the design matrix as

$$X = \begin{pmatrix} B_1 & & & \\ & B_2 & & \\ & & \ddots & \\ & & & B_M \end{pmatrix}, \quad (8)$$

where M is the total number of bands. All of the off-diagonal blocks are filled with zeros. The diagonal blocks share the same ω , while their Fourier coefficients can be different. We perform a grid search on the free parameters in ω and adopt the fit with the least error-weighted residual sum of squares—i.e., the total χ^2 of the fit to the data. Given a trial ω , the regression

Table 5
Sources of the Ground-based VIJH Light Curves

Identifier	References ^a			
	<i>V</i>	<i>I</i>	<i>J</i>	<i>H</i>
S Vul	1, 2	NA	3	3
SS CMa	1, 4	5, 6	NA	7
XY Car	4	8	NA	7
VX Per	9–15	15	3	3
VY Car	5, 13, 16	5, 6	17	7, 17
WZ Sgr	1, 4	5	3, 17	3, 7, 17
X Pup	1, 4	6, 18	17	7, 17

Note.

^a The labels correspond to the following references. 1: Unreleased ASAS (K. Stanek 2018, private communication); 2: Vila observation (S. Engle 2018, private communication); 3: Monson & Pierce (2011); 4: ASAS Pojmanski (1997); 5: Coulson & Caldwell (1985), from McMaster; 6: Berdnikov et al. (2000); 7: CTIO observations; 8: Coulson et al. (1985), from McMaster; 9: Berdnikov (1992a), from McMaster; 10: Szabados (1981), from McMaster; 11: Szabados (1991), from McMaster; 12: Berdnikov (1987), from McMaster; 13: Harris (1980), from McMaster; 14: Berdnikov & Yakubov (1993), from McMaster; 15: Moffett & Barnes (1984), from McMaster; 16: Madore (1975), from McMaster; 17: Laney & Stobie (1992), from McMaster; 18: Berdnikov & Turner (1995), from McMaster; NA: No ground-based light curves, linear interpolation used.

coefficients are solved by

$$\beta = (X^T \Sigma^{-1} X)^{-1} (X^T \Sigma^{-1} Y), \quad (9)$$

where β is the best-fit array of Fourier coefficients, Σ is a rank n diagonal matrix with $\text{Diag}(\Sigma) = \{\sigma^2\}_n$, and $Y = \{m\}_n$ is an $n \times 1$ matrix for the measured magnitudes. The χ^2 is subsequently obtained by

$$\chi^2 = (Y - X\beta)^T \Sigma^{-1} (Y - X\beta). \quad (10)$$

We tried two models to describe ω . The first is a constant-period model with $\omega = 2\pi/p_0$, where p_0 is the period P , while the second is a varying-period model with $\omega = 2\pi/(p_0 + p_1 t)$, where p_0 and p_1 are free parameters. Because these Cepheids are very bright, the values of σ are low and fairly equivalent, so in practice we weigh all of the data equally. We excluded any bands with fewer than 20 measurements, full spans less than a year, or with phase gaps larger than 0.15 from phase determination. The order of the Fourier series for each band was set to approximately one-fourth of the number of measurements n_b , and we restricted the order to be no higher than 7. We found that the period change of S Vul is sufficiently complicated over the time span of collected data that its phase cannot be described by the above simple models. To obtain a better estimation of its phase, we excluded any data older than HJD = 2,454,500 and fit the model only with the data close in time to the *HST* observations. We adopted the varying-period model for all Cepheids except WZ Sgr. The end result of the Fourier model is the Cepheid period or period function. Because light curves in all bands are useful for determining the period or its change, we used a broader set of light-curve data given in Table 6.

Once the observation times are converted to phase using the period or period function, we use a cubic spline to interpolate the light curves and find the magnitude at the observed phase,

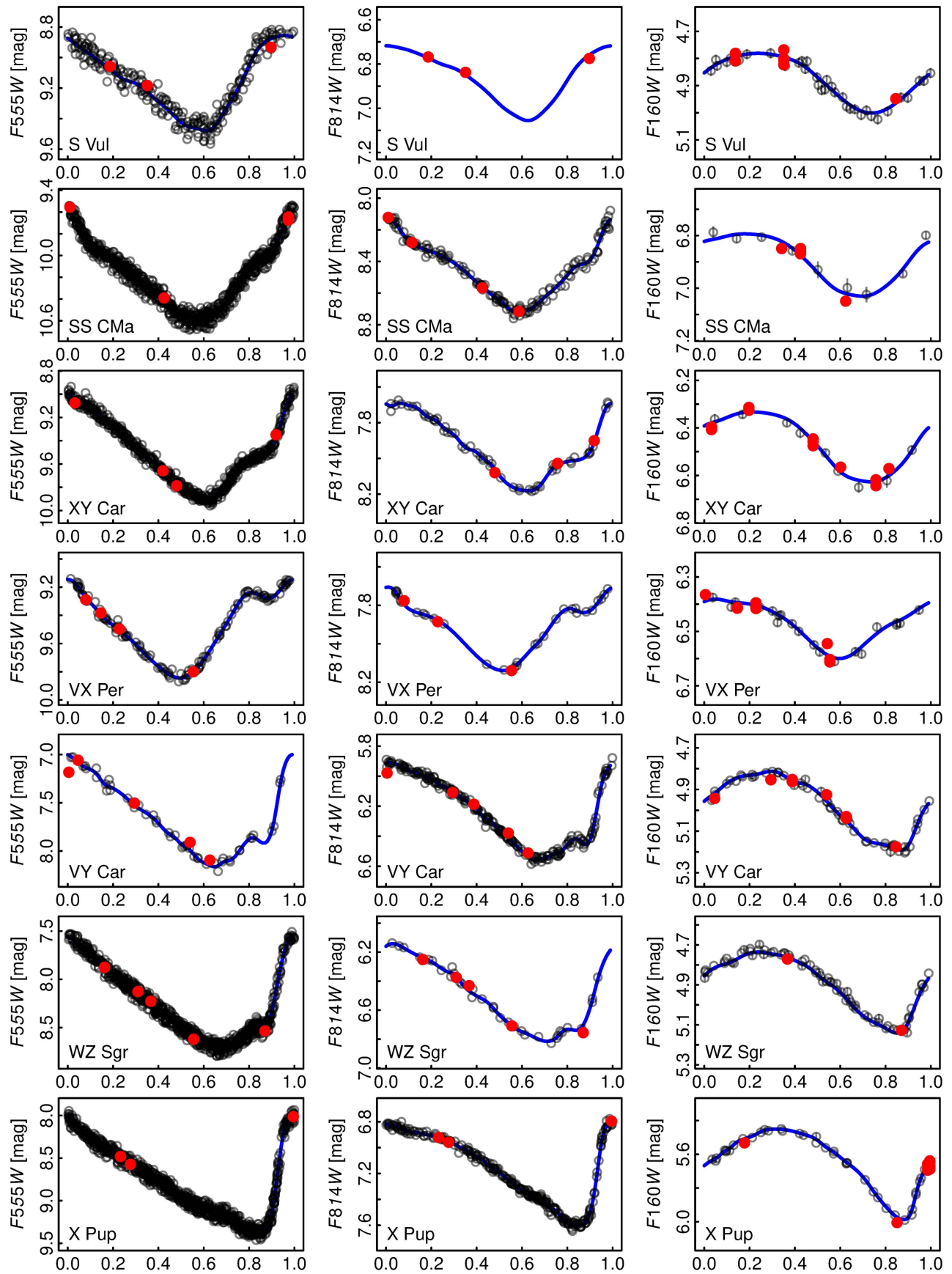


Figure 13. Use of ground-based light curves (transformed to the WFC3 system) to determine the phase correction for the *HST* observations (red points) in $F555W$, $F814W$, and $F160W$.

Table 6
Sources of the Ground Light Curves for Period Determination

Identifier	References ^a	Bands	p_0	p_1	t_{ref}
S Vul	1–17	U, B, V, R_J, H^b	68.96595	2.3362e–04	2455786.6
SS CMa	1, 4, 6, 7, 18, 19	U, B, V, R_C, I_C	12.35586	–2.3166e–07	2449153.6
XY Car	4, 6, 16, 18, 20	U, B, V, R_C, I_C	12.43585	4.6595e–08	2448352.1
VX Per	6, 8, 13, 16, 21–24	V, U, B, R_J	10.88654	–1.7926e–07	2445958.3
VY Car	5, 16–19, 25	$B, V, R_C, I_C, J_{\text{SAAO}}, K_{\text{SAAO}}, H$	18.89843	–1.3034e–06	2449417.1
WZ Sgr	3–7, 12, 16–19, 24, 25	$U, B, V, R_C, I_C, J_{\text{SAAO}}, K_{\text{SAAO}}, R_J, I_J, J_{\text{CTIO}}, K_{\text{CTIO}}, H$	21.85119	NA	2449469.1
X Pup	4–7, 16–18, 24, 26–28	$B, V, J_{\text{SAAO}}, K_{\text{SAAO}}, V_W, B_W, U_W, L_W, H$	25.96749	4.7212e–07	2448872.4

Notes.

^a The labels correspond the following references. 1: Unreleased ASAS (K. Stanek 2018, private communication); 2: RCT observations (S. Engle 2018, private communication); 3: Monson & Pierce (2011); 4: ASAS; Pojmanski (1997); 5: CTIO observations; 6: I-OMC, Alfonso-Garzón et al. (2012); 7: Berdnikov (1986), from McMaster; 8: Berdnikov (1987), from McMaster; 9: Berdnikov (1992b), from McMaster; 10: Berdnikov (1992c), from McMaster; 11: Berdnikov (1992d), from McMaster; 12: Berdnikov (1992e), from McMaster; 13: Berdnikov (1992a), from McMaster; 14: Berdnikov (1993), from McMaster; 15: Berdnikov & Vozyakova (1995), from McMaster; 16: Harris (1980), from McMaster; 17: Laney & Stobie (1992), from McMaster; 18: Madore (1975), from McMaster; 19: Coulson & Caldwell (1985), from McMaster; 20: Coulson et al. (1985), from McMaster; 21: Szabados (1981), from McMaster; 22: Szabados (1991), from McMaster; 23: Berdnikov & Yakubov (1993), from McMaster; 24: Moffett & Barnes (1984), from McMaster; 25: Welch et al. (1984), from McMaster; 26: Berdnikov & Turner (1995), from McMaster; 27: Pel (1976), from McMaster; 28: Welch (1986), from McMaster.

^b Data merged from H_{SAAO} and H_{CTIO} measurements.

m_ϕ . The phase-correction curve \mathcal{C}_ϕ is defined as

$$\mathcal{C}_\phi = \bar{m} - m_\phi,$$

where \bar{m} is the mean magnitude. To transform the phase corrections from the ground-based system to the WFC3 system, we use the color transformations from Riess et al. (2016):

$$\begin{aligned} m_{555} &= V + 0.034 + 0.11(V - I), \\ m_{814} &= I + 0.02 - 0.018(V - I), \\ m_{160} &= H + 0.16(J - H). \end{aligned}$$

We note that the WFC3 phase-correction curves are independent of the zeropoints of the ground-based light curves or the zeropoint transformation between the ground and WFC3, e.g.,

$$\begin{aligned} \mathcal{C}_\phi(F555W) &= (1 + 0.11)\mathcal{C}_\phi(V) - 0.11\mathcal{C}_\phi(I), \\ \mathcal{C}_\phi(F814W) &= (1 + 0.018)\mathcal{C}_\phi(I) - 0.018\mathcal{C}_\phi(V), \\ \mathcal{C}_\phi(F160W) &= (1 - 0.16)\mathcal{C}_\phi(H) + 0.16\mathcal{C}_\phi(J). \end{aligned}$$

For the H band, we fit the templates from Inno et al. (2015) to the data if the number of H -band measurements is fewer than 20 (SS CMa and XY Car). In some cases, there are no ground-based data (I -band data for S Vul, J -band data for SS CMa and XY Car), so we predicted the ground phase-correction curve based on those of the two neighboring bands:

$$\begin{aligned} \mathcal{C}_\phi(m_1) &= a_0 + a_1 \cos(2\pi\phi) + a_2 \sin(2\pi\phi) \\ &\quad + a_3 \mathcal{C}_\phi(m_2) + a_4 \mathcal{C}_\phi(m_3). \end{aligned}$$

The coefficients a_0 – a_4 were derived from least-squares regression over a sample of ~ 50 MW Cepheids. For each HST measurement, we computed its phase Φ with $\Phi = (t \bmod p)/p$, where $p = p_0$ or $p = p_0 + p_1 t$, depending on which ω model is used for the corresponding Cepheid. The mean magnitude is then obtained by adding the phase-correction value $\mathcal{C}_{\phi=\Phi}$ to the HST measurement.

ORCID iDs

Wenlong Yuan <https://orcid.org/0000-0001-9420-6525>
 Lucas Macri <https://orcid.org/0000-0002-1775-4859>
 Jay Anderson <https://orcid.org/0000-0003-2861-3995>

Alexei V. Filippenko <https://orcid.org/0000-0003-3460-0103>

David O. Jones <https://orcid.org/0000-0002-6230-0151>
 Brad E. Tucker <https://orcid.org/0000-0002-4283-5159>

References

- Addison, G. E., Watts, D. J., Bennett, C. L., et al. 2017, arXiv:1707.06547
 Alfonso-Garzón, J., Domingo, A., Mas-Hesse, J. M., & Giménez, A. 2012, *A&A*, 548, A79
 Anderson, R. I., Casertano, S., Riess, A. G., et al. 2016, *ApJS*, 226, 18
 Anderson, R. I., & Riess, A. G. 2017, arXiv:1712.01065
 Aylor, K., Hou, Z., Knox, L., et al. 2017, *ApJ*, 850, 101
 Bellini, A., Anderson, J., & Bedin, L. R. 2011, *PASP*, 123, 622
 Benedict, G. F., McArthur, B. E., Feast, M. W., et al. 2007, *AJ*, 133, 1810
 Berdnikov, L. N. 1986, *PZ*, 22, 369
 Berdnikov, L. N. 1987, *PZ*, 22, 530
 Berdnikov, L. N. 1992a, *SvAL*, 18, 130
 Berdnikov, L. N. 1992b, *A&AT*, 2, 107
 Berdnikov, L. N. 1992c, *A&AT*, 2, 1
 Berdnikov, L. N. 1992d, *A&AT*, 2, 31
 Berdnikov, L. N. 1992e, *A&AT*, 2, 43
 Berdnikov, L. N. 1993, *AstL*, 19, 84
 Berdnikov, L. N., Dambis, A. K., & Vozyakova, O. V. 2000, *A&AS*, 143, 211
 Berdnikov, L. N., & Turner, D. G. 1995, *AstL*, 21, 717
 Berdnikov, L. N., & Vozyakova, O. V. 1995, *AstL*, 21, 308
 Berdnikov, L. N., & Yakubov, S. D. 1993, *PZ*, 23, 47
 Bernal, J. L., Verde, L., & Riess, A. G. 2016, *JCAP*, 10, 019
 Bonvin, V., Courbin, F., Suyu, S. H., et al. 2017, *MNRAS*, 465, 4914
 Bressan, A., Marigo, P., Girardi, L., et al. 2012, *MNRAS*, 427, 127
 Cardona, W., Kunz, M., & Pettorino, V. 2017, *JCAP*, 3, 056
 Casertano, S., Riess, A. G., Anderson, J., et al. 2016, *ApJ*, 825, 11
 Casertano, S., Riess, A. G., Bucciarelli, B., & Lattanzi, M. G. 2017, *A&A*, 599, A67
 Coulson, I. M., & Caldwell, J. A. R. 1985, *SAAOC*, 9
 Coulson, I. M., Caldwell, J. A. R., & Gieren, W. P. 1985, *ApJS*, 57, 595
 DES Collaboration, Abbott, T. M. C., Abdalla, F. B., et al. 2017, arXiv:1711.00403
 Dhawan, S., Jha, S. W., & Leibundgut, B. 2017, arXiv:1707.00715
 Feast, M. W., & Catchpole, R. M. 1997, *MNRAS*, 286, L1
 Feeney, S. M., Mortlock, D. J., & Dalmasso, N. 2017, arXiv:1707.00007
 Follin, B., & Knox, L. 2017, arXiv:1707.01175
 Gatewood, G., de Jonge, K. J., & Stephenson, B. 1993, *PASP*, 105, 1101
 Giménez, A., Mas-Hesse, J. M., Domingo, A., & Omic Consortium 2001, in *ESA Special Publication 459, Exploring the Gamma-Ray Universe*, ed. A. Giménez, V. Reglero, & C. Winkler (Noordwijk: ESA), 375
 Gray, R. O., & Corbally, C. J. 2014, *AJ*, 147, 80
 Hanson, R. B. 1979, *MNRAS*, 186, 875
 Harris, H. C. 1980, PhD thesis, Washington Univ.

- Hubble, E. 1929, *PNAS*, **15**, 168
- Humphreys, E. M. L., Reid, M. J., Moran, J. M., Greenhill, L. J., & Argon, A. L. 2013, *ApJ*, **775**, 13
- Inno, L., Matsunaga, N., Romaniello, M., et al. 2015, *A&A*, **576**, A30
- Jang, I. S., Hatt, D., Beaton, R. L., et al. 2017, arXiv:1703.10616
- Jang, I. S., & Lee, M. G. 2017, *ApJ*, **836**, 74
- Kalirai, J. S., MacKenty, J., Bohlin, R., et al. 2009, WFC3 SMOV Proposal 11451: The Photometric Performance and Calibration of WFC3/IR, Tech. Rep. WFC3 2009-30
- Laney, C. D., & Stobie, R. S. 1992, *A&AS*, **93**, 93
- Lindgren, L., Lammers, U., Bastian, U., et al. 2016, *A&A*, **595**, A4
- Macri, L. M., Ngewo, C.-C., Kanbur, S. M., Mahzooni, S., & Smitka, M. T. 2015, *AJ*, **149**, 117
- Madore, B. F. 1975, *ApJS*, **29**, 219
- Madore, B. F. 1982, *ApJ*, **253**, 575
- Marshall, D. J., Robin, A. C., Reylé, C., Schultheis, M., & Picaud, S. 2006, *A&A*, **453**, 635
- Moffett, T. J., & Barnes, T. G., III 1984, *ApJS*, **55**, 389
- Monson, A. J., & Pierce, M. J. 2011, *ApJS*, **193**, 12
- Oddershov, I., Hannestad, S., & Brandbyge, J. 2017, *JCAP*, **3**, 022
- Oddershov, I., Hannestad, S., & Haugbølle, T. 2014, *JCAP*, **10**, 028
- Pel, J. W. 1976, *A&AS*, **24**, 413
- Persson, S. E., Madore, B. F., Krzeminski, W., et al. 2004, *AJ*, **128**, 2239
- Pietrzyński, G., Graczyk, D., Gieren, W., et al. 2013, *Natur*, **495**, 76
- Planck Collaboration, Aghanim, N., Ashdown, M., et al. 2016, *A&A*, **596**, A107
- Pojmanski, G. 1997, *AcA*, **47**, 467
- Riess, A. G. 2011, An Independent Determination of WFC3-IR Zeropoints and Count Rate Non-Linearity from 2MASS Asterisms, Tech. Rep. WFC3 Instrument Science Report 2011-15
- Riess, A. G., Casertano, S., Anderson, J., MacKenty, J., & Filippenko, A. V. 2014, *ApJ*, **785**, 161
- Riess, A. G., Macri, L. M., Hoffmann, S. L., et al. 2016, *ApJ*, **826**, 56
- Robin, A. C., Reylé, C., Derrière, S., & Picaud, S. 2003, *A&A*, **409**, 523
- Romaniello, M., Primas, F., Mottini, M., et al. 2008, *A&A*, **488**, 731
- Sahu, K., Gosmeyer, C. M., & Baggett, S. 2015, WFC3/UVIS Shutter Characterization, Tech. Rep. Instrument Science Report WFC3 2015-12
- Sesar, B., Fouesneau, M., Price-Whelan, A. M., et al. 2017, *ApJ*, **838**, 107
- Skrutskie, M. F., Cutri, R. M., Stiening, R., et al. 2006, *AJ*, **131**, 1163
- Szabados, L. 1981, CoKon, **77**, 1
- Szabados, L. 1991, CoKon, **96**, 123
- van Leeuwen, F., Feast, M. W., Whitelock, P. A., & Laney, C. D. 2007, *MNRAS*, **379**, 723
- Welch, D. L. 1986, PhD thesis, Univ. Toronto
- Welch, D. L., Wieland, F., McAlary, C. W., et al. 1984, *ApJS*, **54**, 547
- Wielgorski, P., Pietrzynski, G., & Gieren, W. 2017, *EPJWC*, **152** 07011
- Wu, H.-Y., & Huterer, D. 2017, *MNRAS*, **471**, 4946